Impact-generated dust clouds around planetary satellites: spherically symmetric case

Alexander V. Krivov[a,*,1], Miodrag Sremčević[a], Frank Spahn[a], Valeri V. Dikarev[b,1], Konstantin V. Kholshevnikov[c]

[a] *AG "Nichtlineare Dynamik", Institut für Physik, Universität Potsdam, Postfach 601553, 14415 Potsdam, Germany*
[b] *Max-Planck Institut für Kernphysik, Postfach 103980, 69029 Heidelberg, Germany*
[c] *Astronomical Institute, St. Petersburg University, 198504 St. Petersburg, Russia*

Abstract

An analytic model of an impact-generated, steady-state, spherically symmetric dust cloud around an atmosphereless planetary satellite (or planet—Mercury, Pluto) is constructed. The projectiles are assumed to be interplanetary micrometeoroids. The model provides the expected mass, density, and velocity distributions of dust in the vicinities of parent bodies. Applications are made to Jupiter's moon Ganymede and six outer satellites of Saturn. In the former case, the model is shown to be consistent with the measurements of the dust detector system onboard the Galileo spacecraft. In the latter case, estimates are given and recommendations are made for the planned experiment with the Cassini cosmic dust analyzer (CDA) during targeted flybys of the spacecraft with the moons. The best CDA pointing to maximize the number of detections is in the ram direction. With this pointing, measurements are possible within a few to about 20 min from the closest approach, with maximum minute impact rates ranging from about 1 for Phoebe and Hyperion to thousands for Enceladus. Detections of the ejecta clouds will still be likely if CDA's angular offset from the ram direction does not exceed 45°. The same model can be applied to dust measurements by other space missions, like New Horizons to Pluto or BepiColombo to Mercury.
© 2003 Elsevier Science Ltd. All rights reserved.

Keywords: Interplanetary dust; Micrometeoroids; Impact processes; Planetary satellites; Orbital dynamics

1. Introduction

One of the source mechanisms producing dust, especially important in planetary environments, is hypervelocity impacts of micrometeoroids, interstellar grains, or ring particles onto the surfaces of small bodies that lack an atmosphere, such as planetary satellites (Burns et al., 1984), asteroids (Hamilton and Burns, 1991, 1992) or Edgeworth-Kuiper belt (EKB) objects (Jewitt and Luu, 1995; Yamamoto and Mukai, 1998). The same mechanism is expected to work at Mercury (Müller et al., 2002) and at Pluto and Charon (Thiessenhusen et al., 2002). Recent in situ detections of ejecta clouds around Galilean satellites of Jupiter (Krüger et al., 1999, 2000) and future measurements of dust swarms around other bodies (e.g. outer saturnian

moons by the Cassini spacecraft) can be considered as a natural impact experiment in space, extending laboratory impact experiments to a broader range of masses and speeds, astrophysically relevant materials and morphologies of targets and projectiles, and microgravity conditions. Furthermore, future detection and measuring impact rates, masses, and chemical composition of grains with cosmic dust analyzer (CDA), the dust detector aboard Cassini, would yield valuable information on the micrometeoroidal environment in the outer saturnian system and properties of the satellite surfaces. Ultimately, these measurements would provide a deep insight into the dust production and transport in the saturnian system. They could also be crucial to check the hypotheses: that dark Phoebe dust is deposited at the leading hemisphere of Iapetus (Burns et al., 1996); that the material from Phoebe is efficient at ejecting debris from Iapetus and Hyperion (Banaszkiewicz and Krivov, 1997; Krivov and Banaszkiewicz, 2001a, b); that Hyperion's icy ejecta are largely responsible for the influx of water molecules on

---

*Corresponding author.
E-mail address: krivov@agnld.uni-potsdam.de (A.V. Krivov).
[1] On leave from: Astronomical Institute, St. Petersburg University, Russia.

Titan, explaining the observed abundances of CO and CO_2 molecules in its atmosphere (Banaszkiewicz and Krivov, 1997; Krivov and Banaszkiewicz, 2001a, b).

In this paper, we construct a model of a spherically symmetric impact-generated dust cloud around a celestial body which lacks a gaseous atmosphere. The model provides the mass, density, and velocity distributions of dust in the vicinities of parent bodies. Applications are made to the largest jovian satellite, Ganymede, and to six outer saturnian satellites—from Enceladus to Phoebe. In the former case, the model is shown to be consistent with the measurements of the dust detector onboard the Galileo spacecraft. In the latter case, we provide estimates and make recommendations for the Cassini CDA experiment planning for targeted flybys of the moons.

The paper is organized as follows. The model consists of two parts: description of the dust production from a satellite (Section 2) and derivation of the steady-state distribution of the ejected particles around it (Section 3). Accordingly, in Section 2, we describe the mechanism of the dust production and estimate the production rate, mass and speed distribution of the ejecta from the surfaces of satellites. In Section 3, we derive spatial and velocity distributions of dust in a spherically symmetric dust cloud around a moon. The reader interested in applying the model and not in math details may want to skip Sections 2.1–2.3 and 3.1–3.3 and to proceed directly to Sections 2.4 and 3.4 where a summary of the two parts of the model is given. In Section 4.1, the model is applied to the dust cloud around Ganymede and the modeling results are compared to the Galileo dust detector system (DDS) measurements. In Section 4.2, applications to outer Saturn's satellites are made. Here, the number density of grains at different distances from the moons is calculated and expectations for the Cassini CDA experiment are discussed. In Section 5, we analyze the velocity dispersion of dust grains in the dust clouds of the saturnian moons and use the results to discuss the dependence of the impact fluxes on the Cassini CDA orientation. Section 6 lists our conclusions.

2. Model of a dust cloud: dust production rate from a satellite surface

2.1. Mass flux and speed of impactors

In this paper, we assume that the dust material is kicked off the surfaces of the moons by hypervelocity impacts of interplanetary meteoroids. The interplanetary dust environment at the heliocentric distances of Jupiter and Saturn has been probed by a few spacecraft; many of their data were incorporated in Divine's (1993) model. We have calculated the fluxes of interplanetary grains onto spheres with unit cross section ($\pi R^2 = 1$), moving around the Sun in circular Keplerian orbits with radii of 5.2 and 9.5 AU (heliocentric distances of Jupiter and Saturn). Fig. 1 depicts, as a function of particle's mass, the cumulative flux onto these spheres,
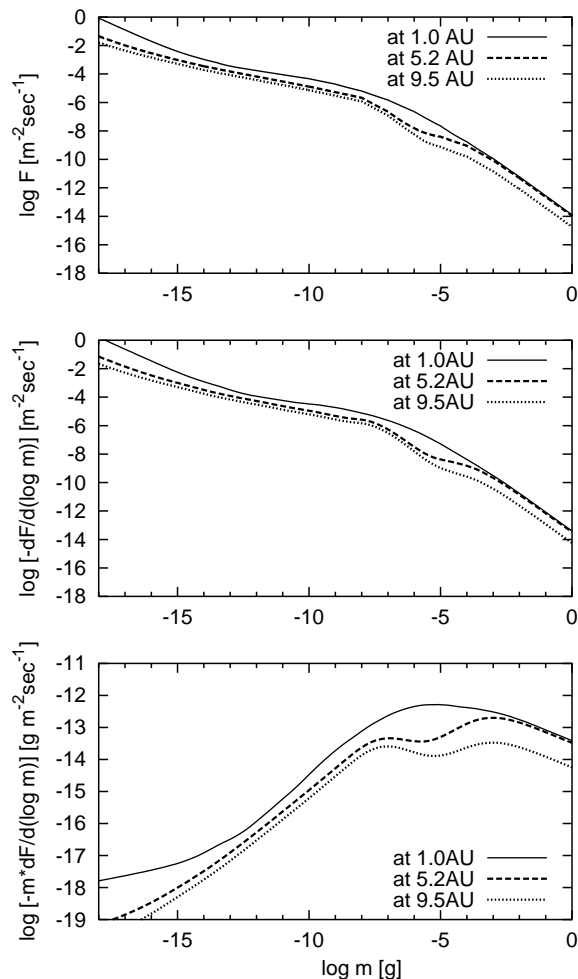

Fig. 1. Fluxes of interplanetary grains onto a sphere with unit cross section ($\pi R^2 = 1$), moving around the Sun in a circular Keplerian orbit with radius of 1.0 AU (—), 5.2 AU (- - -), and 9.5 AU (...), according to Divine's (1993) model. Top: the cumulative flux; middle: the differential flux per unit log mass interval; bottom: the differential mass flux per unit log mass interval. Dips of the dashed and dotted curves at masses $\sim 10^{-5}$ g are probably artefacts of the Divine's model rather than a real property of the dust fluxes, reflecting the scarcity of the dust detector data on which the model is based.

the differential flux per mass decade, as well as the differential mass flux per mass decade. For comparison, the same fluxes at 1 AU are also shown.

The model suggests that at Jupiter's heliocentric distance the *mass flux of impactors* is

$$F_{imp}^{\infty} = 7.6 \times 10^{-17} \ g \ cm^{-2} \ s^{-1}, \tag{1}$$

whereas at Saturn's distance

$$F_{imp}^{\infty} = 1.8 \times 10^{-17} \ g \ cm^{-2} \ s^{-1}. \tag{2}$$

Here, the superscript ∞ indicates that this is a value of the impactor flux "far" from Jupiter or Saturn. Below it will be corrected for the gravitational focusing by the planet. In both cases, the mass flux is dominated by grains with

masses $\sim 10^{-5}$ g (or with sizes ~ 100 µm for a 2 g cm^{-3} bulk density) that belong to the "asteroidal population" (low eccentricities, low inclinations) and "halo population" (moderate eccentricities, broadly distributed inclinations) in the terminology of Divine.

It should be emphasized that the interplanetary environment in the outer Solar system is poorly known. For instance, the only dust data available at Saturn's heliocentric distance came from the dust detectors of Pioneer 10/11 spacecraft (Humes, 1980), for which a number of reservations exist (e.g., Dikarev and Grün, 2002). As a result, the mass fluxes reported are very uncertain. Grün et al. (1985) model gives a smaller value of $F_{imp}^{\infty} = 2.6 \times 10^{-18}$ g cm^{-2} s^{-1} (Banaszkiewicz and Krivov, 1997), another method used in Thiessenhusen et al. (2002) yields a higher estimate $F_{imp}^{\infty} = 2.4 \times 10^{-16}$ g cm^{-2} s^{-1}, whereas Cuzzi and Durisen (1990) and Cuzzi and Estrada (1998) have settled on the value $F_{imp}^{\infty} = 5 \times 10^{-17}$ g cm^{-2} s^{-1}. Thus, values (1) and (2) have probably about a factor of 10 uncertainty.

Apart from the mass fluxes, we need to know *velocities of the impacting micrometeoroids*. We calculated the mean velocities of interplanetary dust particles (IDPs) with the same model (Divine, 1993). The (mass-weighted) average velocity of IDPs relative to a unit sphere moving in a circular heliocentric Keplerian orbit is

$$v_{imp}^{\infty} = 9.0 \text{ km s}^{-1} \tag{3}$$

at Jupiter and

$$v_{imp}^{\infty} = 9.5 \text{ km s}^{-1} \tag{4}$$

at Saturn. The superscript ∞ reminds again that these values are still to be corrected for the gravitational focusing by a planet at the satellite distance from it. The reason for the velocity to be slightly higher at Saturn than at Jupiter is that, of the two dominant IDP populations (asteroidal with mean velocity of 5–7 km s^{-1} and halo with mean velocity of 15–21 km s^{-1}), the relative contribution of the halo particles at Saturn is somewhat higher than at Jupiter.

The velocities of IDPs in the outer Solar system are as vaguely known as are the fluxes. Instead of using Divine's empirical model, Colwell and Horányi (1996) suggested to consider two limiting cases that are likely to "bracket" the reality: (i) a low-e, low-i "planetary" population of particles that are likely to come from the EKB, and (ii) an "Oort cloud" population of highly eccentric, randomly inclined particles that could be supplied by long-period comets. At Jupiter, their calculations give the velocities of the impactors in the range from 6 to 10 km s^{-1} with the mean of 6.6 km s^{-1} (planetary population) and from 8 to 34 km s^{-1} with the mean of 23.6 km s^{-1} (Oort cloud population). This example shows that the likely uncertainty of values (3) and (4) is about a factor of 2.

We have to take into account the *gravitational focusing by a planet*. The effect has two consequences: at each of the moons, (i) the speed of the grains v_{imp} becomes larger than that far from the planet, v_{imp}^{∞}, and (ii) the spatial density of dust n_{imp} gets larger than the one far from the planet, n_{imp}^{∞}. Assuming v_{imp}^{∞} given above and applying the energy integral, we can find v_{imp}, the mean velocity of impactors with respect to the *planet* at the moon distance a. Since the incoming directions of the projectiles are broadly distributed, whereas the direction of the moon orbital velocity changes periodically, we can roughly take this value as the mean projectile velocity with respect to the *moon*. We note, however, that the velocities of individual grains striking the satellite may have a very large dispersion. This would result in a non-uniform and time-dependent dust production from the surface and, as a consequence, in an asymmetric and time-variable dust density distribution in the dust cloud (Colwell, 1993). These effects are the subject of a subsequent paper.

The ratio v_{imp}/v_{imp}^{∞} is calculated from the energy integral

$$\frac{v_{imp}}{v_{imp}^{\infty}} = \sqrt{1 + \frac{2GM_p}{a(v_{imp}^{\infty})^2}}, \tag{5}$$

where G is the gravitational constant and M_p is the planet mass. An expression for n_{imp}/n_{imp}^{∞} was derived by Colombo et al. (1966). Their Eq. (11) gives

$$\frac{n_{imp}}{n_{imp}^{\infty}} = \frac{1}{2} \left[\left(1 + \frac{2GM_p}{a(v_{imp}^{\infty})^2} \right)^{1/2} + 1 \right]$$

$$\times \left[1 + \frac{2GM_p}{a(v_{imp}^{\infty})^2} - \left(\frac{R_p}{a} \right)^2 \left(1 + \frac{2GM_p}{R_p(v_{imp}^{\infty})^2} \right) \right]^{1/2} \tag{6}$$

with R_p being the radius of the planet. This equation is valid if

$$v_{imp}^{\infty} > \sqrt{\frac{2GM_p a}{R_\Sigma^2 - a^2}}, \tag{7}$$

where R_Σ is the radius of the planet's sphere of influence with respect to the Sun. Eq. (7) is always fulfilled for the jovian and saturnian cases considered in this paper. Then,

$$\frac{F_{imp}}{F_{imp}^{\infty}} = \frac{v_{imp}}{v_{imp}^{\infty}} \frac{n_{imp}}{n_{imp}^{\infty}}. \tag{8}$$

The values of v_{imp}/v_{imp}^{∞}, n_{imp}/n_{imp}^{∞}, and F_{imp}/F_{imp}^{∞} are given in Table 1.

We restate that here a "conservative" model is considered: it assumes the interplanetary grains to be the only impactors that strike the satellite surfaces. This may lead, in some cases, to a significant underestimation of the ejecta production rate. At Enceladus, the E-ring impactors can be efficient as well (Spahn et al., 1999). At Hyperion, the Phoebe impactors may play a significant role—even more significant than the interplanetary ones. Banaszkiewicz and Krivov (1997) and Krivov and Banaszkiewicz (2001a) give

Table 1
Speed and flux of impactors after a correction for the gravitational focusing

Satellite	$a(R_p)$	v_{imp}/v_{imp}^∞	n_{imp}/n_{imp}^∞	F_{imp}/F_{imp}^∞	v_{imp} (km s^{-1})	F_{imp} (g cm^2 s^{-1})
Ganymede	15.1	2.0	2.9	5.8	18	4.4×10^{-16}
Enceladus	4.0	2.1	3.2	6.8	20	1.2×10^{-16}
Dione	6.3	1.8	2.5	4.4	17	7.9×10^{-17}
Rhea	8.7	1.6	2.1	3.4	15	6.1×10^{-17}
Hyperion	24.6	1.3	1.4	1.8	12	3.2×10^{-17}
Iapetus	59.0	1.1	1.2	1.3	11	2.3×10^{-17}
Phoebe	215	1.03	1.05	1.08	10	1.9×10^{-17}

Table 2
Geometric albedo, assumed silicate content, energy partitioning parameter, characteristic yield, and parameters of the ejecta speed distribution for different satellites

Satellite	Geom. albedo	G_{sil}	K_e/K_i (%)	Y	u_0 (m s^{-1})	γ
Ganymede	0.4	30	30	4×10^3	40	1.7
Enceladus	0.99	0	30	2×10^4	30	2.0
Dione	0.7	0	30	1×10^4	31	2.0
Rhea	0.7	0	30	8×10^3	31	2.0
Hyperion	0.2	70	20	4×10^2	55	1.4
Iapetus	0.2	70	20	3×10^2	57	1.4
Phoebe	0.06	100	10	1×10^2	50	1.2

an estimate of the impactor flux from Phoebe particles of $F_{imp} = 4 \times 10^{-16}$ g cm^{-2} s^{-1}—by one order of magnitude greater than that of the interplanetary impactors. Furthermore, yet another impactor population can be supplied by the other, recently discovered, small irregular moons of Saturn (Gladman et al., 2001).

2.2. Yield, mass distribution, and production rate of ejecta

We start with the *ejecta yield* Y, defined as the ratio of the total ejecta mass to the mass of impactors. We use the experimental data from Koschny and Grün (2001) for ice-to-silicate mixtures as targets. Eq. (7) of Koschny and Grün (2001) (see also their Fig. 10) gives Y as a function of: the fraction of silicate in the material of the target G_{sil}(0%=pure ice, 100%=pure silicate); speed of impactors v_{imp}; and the typical impactor mass m_{imp}. In SI units,

$$Y = 2.85 \times 10^{-8} \times 0.0149^{G_{sil}/100}$$
$$\times \left(\frac{1 - G_{sil}/100}{927} + \frac{G_{sil}/100}{2800} \right)^{-1} m_{imp}^{0.23} v_{imp}^{2.46}. \quad (9)$$

We approximate the satellite surfaces by ice-to-silicate mixtures with different mass fraction of silicate, choosing the latter in accordance with the surface albedo. For bright Enceladus, Dione, and Rhea, pure ice ($G_{sil} = 0\%$) is assumed, for very dark Phoebe, pure silicate ($G_{sil} = 100\%$) is taken, whereas for other moons, intermediate values are used (Table 2). Taking v_{imp} from Table 1 and $m_{imp} \sim 10^{-5}$ g as

typical impactor's mass (≈ 100 μm in radius), we get the values listed in Table 2. The yield ranges from $Y \approx 1 \times 10^2$ (Phoebe) to 2×10^4 (Enceladus).

The *mass production rate* from the surface is

$$M^+ = F_{imp} Y S \quad (10)$$

with $S = \pi r_M^2$ being the cross section area of the moon of radius r_M. The fact that S in Eq. (10) is the *cross section* πR^2 and not the *surface area* $4\pi R^2$ of the satellite is not trivial and needs to be explained. Tublina and Kholshevnikov (1991) considered a convex body with the surface area σ in an n-dimensional Euclidean space $\mathbf{R}^n$, placed in a field of particles with an isotropic velocity distribution, and found the accretion rate to be $F_{imp} S$, where $S\sigma = V_{n-1}/(nV_n)$ and V_n is the volume of an n-dimensional sphere of a unit radius. For $n = 3$ and a spherical body, we get $\sigma = 4\pi r_M^2$, $V_{n-1} = \pi$ and $V_n = 4\pi/3$, resulting indeed in $S = \pi r_M^2$. Qualitatively, this result is a "projection effect": an isotropic field of impactors consists of particles moving in all possible directions and, no matter which direction an impactor has, it "sees" only the cross section of the body, which is $S = \pi r_M^2$.

Since $Y \propto v_{imp}^{2.5}$ (Eq. (9)) and $F_{imp} \propto v_{imp}$, Eq. (10) predicts a strong dependence of the dust production rate on the impact velocity: $M^+ \propto v_{imp}^{3.5}$. Kholshevnikov and Shor (1994, 1995) have shown that $\langle v_{imp}^q \rangle$ (angular brackets denote mathematical expectation) exceeds $\langle v_{imp} \rangle^q$ for $q > 1$. In our case, using Eq. (10) may lead to underestimation of the production rate by 10–20%. Thus, the effect is not significant, keeping in mind large uncertainties in the model parameters.

A *mass distribution of the debris* is taken to be a power law. Namely, the number of grains with masses $> M_{min}$ ejected from the satellite surface per unit time is expressed as

$$N^+(> M_{min}) = \frac{1 - \alpha}{\alpha} \frac{M^+}{M_{max}} \left(\frac{M_{max}}{M_{min}} \right)^\alpha, \quad (11)$$

which introduces two more parameters: maximum mass of an ejected fragment M_{max} and the distribution slope α.

The results depend on M_{max} only weakly (Krüger et al., 2000). We assume it to be close to the typical mass of an impactor

$$M_{max} = 1 \times 10^{-5} \text{ g.} \quad (12)$$

Table 3
Galileo and Cassini encounter distances, speeds, DDS/CDA thresholds (velocity-dependent, hence different for different flybys), and production rate of grains with masses greater than the DDS or CDA threshold from the satellite surfaces

Satellite and flyby	Distance (r_{M})	Enc. speed (km s^{-1})	Mass threshold (g)	N^+(s^{-1})
Ganymede G1	1.3	7.8	1.1×10^{-13}	2.2×10^{16}
Ganymede G2	1.1	8.0	1.0×10^{-13}	2.4×10^{16}
Ganymede G7	2.2	8.5	8.3×10^{-14}	2.8×10^{16}
Ganymede G8	1.6	8.6	7.9×10^{-14}	2.9×10^{16}
Enceladus1	3.0	6.4	6.0×10^{-14}	3.6×10^{14}
Enceladus2	5.0	8.1	2.4×10^{-14}	7.5×10^{14}
Enceladus3	5.0	14.6	2.4×10^{-15}	4.4×10^{15}
Dione	2.8	9.0	1.6×10^{-14}	2.1×10^{15}
Rhea	1.7	7.3	3.6×10^{-14}	1.3×10^{15}
Rhea-5500	8.5	6.7	5.0×10^{-14}	9.8×10^{14}
Hyperion	8.0	5.6	1.0×10^{-13}	5.2×10^{11}
Iapetus	2.4	2.4	2.8×10^{-12}	5.0×10^{11}
Phoebe	19.2	6.4	6.0×10^{-14}	6.8×10^{10}

Plausible slopes α are between 0.5 and 1.0 (see, e.g., a discussion and references in Krivov and Jurewicz, 1999). In general, a slope close to 0.8 is known to be typical of many physical systems where cratering and/or catastrophic impacts play a dominant role (see, e.g., Krivov et al., 2000). Furthermore, in situ measurements of the ejecta from Ganymede (Krüger et al., 2000) and Europa and Callisto (Krüger et al., 2002) yield similar slopes. We adopt, therefore,

$$\alpha = 0.8. \qquad (13)$$

Throughout the paper, we will take as $M_{\min}$ the velocity-dependent mass threshold of a spacecraft detector, DDS of Galileo or CDA of Cassini. The thresholds are approximated as (Grün et al., 1995; R. Srama, pers. comm.)

$$\frac{M_{\min}}{1\ \mathrm{g}} = 1.5 \times 10^{-10} \left(\frac{v}{1\ \mathrm{km\ s^{-1}}} \right)^{-3.5} \qquad (14)$$

and

$$\frac{M_{\min}}{1\ \mathrm{g}} = 8.4 \times 10^{-11} \left(\frac{v}{1\ \mathrm{km\ s^{-1}}} \right)^{-3.9}, \qquad (15)$$

respectively. Here v is the mean impact speed of the dust grains onto the detector. Taking into account that the speeds of the dust grains relative to a satellite are much less than the speed of a spacecraft with respect to the moon (see subsequent section for numerical estimates), for each of the flybys, we take v to be the encounter speed of a spacecraft. The flyby distances, encounter speeds, and the corresponding mass thresholds from Eqs. (14) and (15) are listed in Table 3. For instance, for a typical Cassini encounter speed of 5 km s^{-1}, the CDA threshold is about $M_{\min} = 1.6 \times 10^{-13}$ g (or about 0.3 μm in terms of radius for a 2 g cm^{-3} bulk density). The production rates N^+ of the ejecta from the satellite surfaces, having masses above the DDS or CDA threshold, were then calculated from Eq. (11). The results are given in Table 3 (last column).

It should be noted that most recent laboratory recalibration of the CDA instrument (Srama et al., 2002) suggests a CDA threshold different from Eq. (15):

$$\frac{M_{\min}}{1\ \mathrm{g}} = 3.04 \times 10^{-10} \left(\frac{v}{1\ \mathrm{km\ s^{-1}}} \right)^{-3.75}, \qquad (16)$$

implying that the CDA sensitivity may be by up to 1 order of magnitude lower than that given by Eq. (15). However, laboratory investigations of CDA are not completed yet. For this reason, in what follows we use Eq. (15). In any case, our results can easily be rescaled for any other detector threshold formula, using the proportionality of dust densities and fluxes to $M_{\min}^{-\alpha}$ (Eq. (11)).

2.3. Ejecta velocity distribution

For an *initial speed distribution of ejecta*, we adopt the following form:

$$f_u(u) = \frac{\gamma}{u_0} \left(\frac{u}{u_0} \right)^{-\gamma-1} H(u - u_0) \qquad (17)$$

with normalization

$$\int_0^\infty f_u(u)\, \mathrm{d}u = 1 \qquad (18)$$

and two parameters, the slope γ and the minimum ejecta speed u_0. In Eq. (17), $H(x)$ is the Heaviside step function equal to 1 for positive arguments and to 0 otherwise.

To choose plausible values of γ, we use the assumed silicate content G_{sil}. For "pure" ice (Enceladus, Dione, Rhea), a reasonable "hard-surface" value of γ is 2.0. For regolith-like targets (Phoebe), $\gamma = 1.2$ is more plausible. For other moons, intermediate values are taken (Table 2).

Another parameter of the ejecta speed distribution, u_0, can be estimated from the energy balance (Krüger et al., 2000). The ratio of the kinetic energy partitioned to the ejecta, K_e, to the impactor's kinetic energy, K_i, must be less than unity,
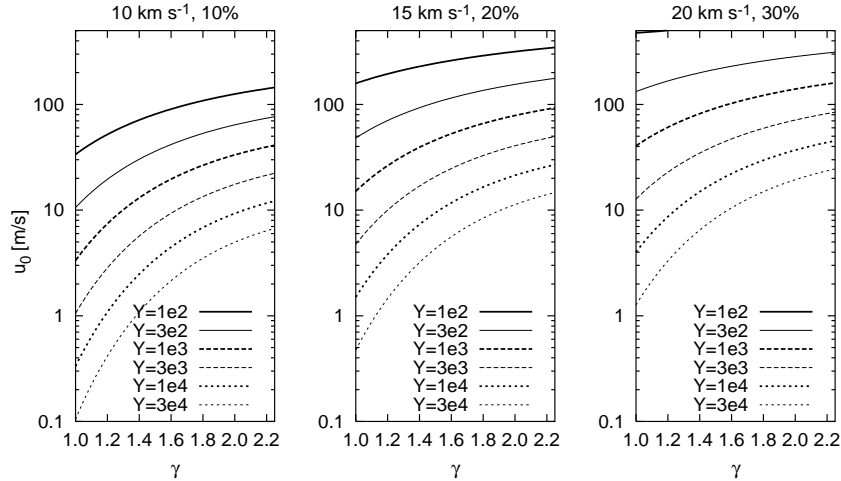
Fig. 2. Energy constraint on the yield Y and parameters u_0, γ of the ejecta speed distribution for three speeds of impactors and kinetic energy fractions ($v_{\mathrm{imp}} = 10$ km s^{-1}, $K_e/K_i = 10\%$, left; $v_{\mathrm{imp}} = 15$ km s^{-1}, $K_e/K_i = 20\%$, middle; $v_{\mathrm{imp}} = 20$ km s^{-1}, $K_e/K_i = 30\%$, right).
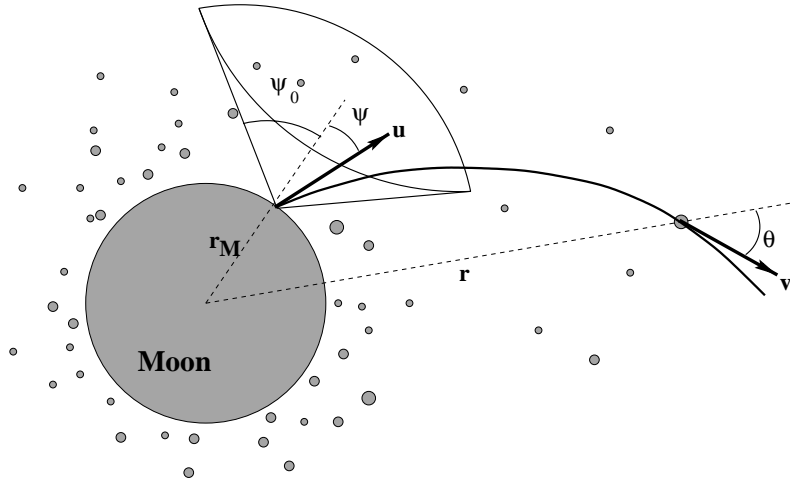

Fig. 3. Geometry of the dust ejection.

because part of K_i is spent for comminution and heating. The ratios K_e/K_i determined in hypervelocity impact experiments vary from a few percent to several tens of percent (see, e.g., Asada, 1985; Hartmann, 1985; and references therein) and are larger for higher impact velocities and for hard surfaces. Accordingly, we assign $K_e/K_i = 0.3$ to Ganymede and saturnian satellites from Enceladus to Rhea, 0.2 to Hyperion and Iapetus, and 0.1 to Phoebe (Table 2).

Calculations described in Krüger et al. (2000) give then a relation between Y, γ and u_0:

$$K_e/K_i = Y \frac{\gamma}{2-\gamma} \left(\frac{u_0}{v_{\mathrm{imp}}} \right)^2 \left[\left(\frac{u_0}{u_{\max}} \right)^{\gamma-2} - 1 \right] \quad (\gamma \neq 2) \tag{19}$$

or

$$K_e/K_i = 2Y \left(\frac{u_0}{v_{\mathrm{imp}}} \right)^2 \ln \frac{u_{\max}}{u_0} \quad (\gamma = 2), \tag{20}$$

where $u_{\max}$ is the maximum ejecta velocity, which we take to be 3 km s^{-1} in the numerical calculations.

Taking v_{imp} from Table 1, and Y from Table 2, Eqs. (19) and (20) can be solved for u_0. Results for three typical cases ($v_{\mathrm{imp}} = 20$ km s^{-1}, $K_e/K_i = 30\%$ for Enceladus; $v_{\mathrm{imp}} = 15$ km s^{-1}, $K_e/K_i = 30\%$; $v_{\mathrm{imp}} = 10$ km s^{-1}, $K_e/K_i = 10\%$ for Phoebe) are plotted in Fig. 2. Full sets of parameters for all satellites, including u_0, are given in Table 2.

We now consider the *angular distribution of the ejecta*. We assume that the grains are ejected uniformly within a cone with an opening angle $\psi_0 \in [0°, 90°]$ (Fig. 3). Thus, the distribution of ψ (the angle between the initial velocity vector and the normal to the satellite surface at the ejection point) is

$$f_\psi(\psi) = \frac{\sin \psi}{1 - \cos \psi_0} H(\psi_0 - \psi). \tag{21}$$

The function $f_\psi(\psi)$ has the following normalization:

$$\int_0^{\pi/2} f_\psi(\psi)\,\mathrm{d}\psi = 1. \tag{22}$$

There are two limiting cases: one when all the particles are ejected normally to the surface, so that $\psi_0 = 0$ or $f_\psi(\psi) = \delta(\psi)$; and another one when the grains are ejected isotropically into the half-space above the "local horizon", $\psi_0 = \pi/2$.

2.4. Summary

In the first part of the model, we used Divine's (1993) model to estimate the mass flux and speed of interplanetary impactors at Jupiter and Saturn and the algorithm of Colombo et al. (1966) to correct them for gravitational focusing.

We then derived the mass production rate from the surface of a satellite, M^+ (Eq. (10)), and the number of grains with masses $> M_{\min}$ ejected from the satellite surface per unit time, $N^+(> M_{\min})$ (Eq. (11)). For initial mass and speed distribution of the ejecta, we assumed power laws (Eqs. (11) and (17), respectively). For initial distribution of the velocity directions, a uniform ejection within a cone normal to the surface (Eq. (21)) was postulated.

Assumed and resulting numerical values for Ganymede and six saturnian moons are given in Tables 2 and 3. In these tables, we take $M_{\min}$ to be the mass threshold of the Galileo and Cassini dust detectors for particular satellite flybys (Eqs. (14) and (15)).

3. Model of a dust cloud: distribution of dust

3.1. Assumptions

Consider a spherically symmetric satellite with the radius r_M and mass M, producing dust grains at a constant rate N^+ (Eqs. (10) and (11) and Table 3). We assume that the particles are uniformly ejected from the whole surface of a satellite and that the ejecta from each surface point go uniformly into a cone around the normal to the surface. The initial velocity distribution of the ejecta (i.e. distribution of speed u and velocity angle ψ) is given by functions $f_u(u)$ and $f_\psi(\psi)$ (Eqs. (17) and (21)).

Further on we will assume that other forces, besides the moon gravity, are negligible in close vicinity of the moon (inside its Hill sphere), and the particles are moving in Keplerian orbits. This assumption should be taken with care. Estimates show that, for the Ganymede ejecta, the Lorentz force due to the recently discovered intrinsic magnetic field of the satellite (Kivelson et al., 1998) may lead to noticeable effects. For Enceladus ejecta at planned flyby distances, the tidal gravity of Saturn, inertial forces and even the Lorentz force arising from the planetary magnetic field may all be of importance (Spahn et al., 1999). For Dione, the tidal gravity of the planet may introduce some corrections. For Phoebe,

the radiation pressure effects may be important (cf. Krivov and Jurewicz, 1999, who considered similar effects on the dust clouds around Phobos and Deimos). Finally, Hyperion may imply complications due to its irregular shape.

3.2. Phase distribution function

Introduce the phase space distribution function $n(\vec{r},\vec{v})$ such that

$$\mathrm{d}n = n(\vec{r},\vec{v})\,\mathrm{d}^3\vec{r}\,\mathrm{d}^3\vec{v} \tag{23}$$

is the number of ejected particles in the unit volume of phase space. In spherical coordinates, let (r,θ_r,λ_r) be components of $\vec{r}$ and (v,θ,λ) be components of $\vec{v}$ (Fig. 3). The symmetries of the problem suggest that the phase distribution depends only on three out of six arguments:

$$n(\vec{r},\vec{v}) \equiv n(r,\theta_r,\lambda_r,v,\theta,\lambda) \equiv n(r,v,\theta). \tag{24}$$

The number of particles at distances $[r,r+\mathrm{d}r]$, moving with speeds $[v,v+\mathrm{d}v]$ at angles $[\theta,\theta+\mathrm{d}\theta]$ with respect to the normal to the surface, is expressed as

$$\mathrm{d}n = n(r,v,\theta)4\pi r^2\,\mathrm{d}r\,2\pi v^2\,\mathrm{d}v\sin\theta\,\mathrm{d}\theta. \tag{25}$$

The phase distribution function $n(r,v,\theta)$ is to be found from the initial distribution function $f(u,\psi)=f_u(u)f_\psi(\psi)$.

Consider a spherical shell of radius r and thickness $\mathrm{d}r$. The number of particles in the shell is $\mathrm{d}n = N^+\,\mathrm{d}t\,\mathrm{d}p$, where N^+ is the total number of grains ejected per unit time, $\mathrm{d}t(r)$ is the time a particle spends in the shell, and $\mathrm{d}p = f\,\mathrm{d}u\,\mathrm{d}\psi$ is the probability that the particle has an initial velocity $u \in [u,u+\mathrm{d}u]$ and $\psi \in [\psi,\psi+\mathrm{d}\psi]$. We then write

$$\mathrm{d}n = N^+\,\mathrm{d}t\,f(u,\psi)\mathrm{d}\psi\,\mathrm{d}u. \tag{26}$$

Equating expressions (25) and (26) yields

$$n(r,v,\theta) = \frac{N^+}{8\pi^2}\frac{1}{r^2}\frac{1}{|\dot{r}|}\frac{1}{v^2\sin\theta}f(u,\psi)\left|\frac{\partial(u,\psi)}{\partial(v,\theta)}\right|, \tag{27}$$

where we introduced the Jacobian of a transformation $(u,\psi) \rightarrow (v,\theta)$. For a given initial ejection velocity at the surface of the moon, a particle in a Keplerian orbit at a position r can have two possible velocities: (v,θ) and $(v,\pi-\theta)$, $\theta \leqslant \pi/2$. This property can be easily verified by using integrals of motion. If we drop for the time being the second case which is symmetric to the first one, transformation $(u,\psi) \rightarrow (v,\theta)$ is unique and properly defined. Then $|\dot{r}| = v\cos\theta$.

From the integrals of motion, those of mechanical energy and angular momentum, we can obtain the transformation rule. For simplicity, we set the mass of a dust grain to unity. At the surface, the mechanical energy and angular momentum read as

$$E_m = \frac{u^2}{2} - \frac{GM}{r_M},\ |\vec{L}| = r_M u\sin\psi, \tag{28}$$

and at the position r

$$E_m = \frac{v^2}{2} - \frac{GM}{r}, |\vec{L}| = rv \sin \theta. \qquad (29)$$

Next, we scale radial coordinates with the radius of the moon r_M and velocities with the surface escape velocity $v_{esc} = \sqrt{2GM/r_M}$, and introduce new variables $\tilde{r}$, $\tilde{u}$ and $\tilde{v}$:

$$\tilde{r} = r/r_M, \tilde{u} = u/v_{esc}, \tilde{v} = v/v_{esc}. \qquad (30)$$

Expression (25) becomes

$$dn = n(\tilde{r}, \tilde{v}, \theta) 4\pi r_M^3 \tilde{r}^2 \, d\tilde{r} \, 2\pi v_{esc}^3 \tilde{v}^2 \, d\tilde{v} \sin \theta \, d\theta. \qquad (31)$$

From (28) and (29), one gets transformation rules

$$\tilde{u}^2 - 1 = \tilde{v}^2 - \frac{1}{\tilde{r}}, \tilde{u} \sin \psi = \tilde{r}\tilde{v} \sin \theta, \qquad (32)$$

or

$$\tilde{u}(\tilde{v}) = \sqrt{\tilde{v}^2 + 1 - \frac{1}{\tilde{r}}}, \psi(\tilde{v}, \theta) = \arcsin\left[\frac{\tilde{r}\tilde{v}}{\tilde{u}(\tilde{v})} \sin \theta\right]. \qquad (33)$$

The Jacobian is

$$J = \left| \frac{\partial(u, \psi)}{\partial(v, \theta)} \right| = \frac{\partial \tilde{u}}{\partial \tilde{v}} \frac{\partial \psi}{\partial \theta} = \frac{\tilde{v}}{\tilde{u}} \frac{\tilde{r}\tilde{v} \cos \theta}{\tilde{u} \cos \psi}. \qquad (34)$$

The phase space distribution function (27) is then

$$n(\tilde{r}, \tilde{v}, \theta) = \frac{N^+}{8\pi^2 r_M^2 v_{esc}^3} \frac{1}{\tilde{r}\tilde{v}\tilde{u}^2 \sin \theta \cos \psi} f(v_{esc}\tilde{u}, \psi), \qquad (35)$$

where $\tilde{u}(\tilde{v})$ and $\psi(\tilde{v}, \theta)$ are calculated from (33). Thus the distribution function, even in general case, is given by a closed analytic formula (35). Note that for an initial velocity $(\tilde{u}, \psi)$ not all pairs $(\tilde{v}, \theta)$ at distance $\tilde{r}$ are possible; this will be discussed in the next section. For a uniform space angle distribution (21) we get

$$n(\tilde{r}, \tilde{v}, \theta) = \frac{N^+}{8\pi^2 r_M^2 v_{esc}^4} \frac{\gamma \tilde{u}_0^\gamma}{1 - \cos \psi_0}$$

$$\times H[\psi_0 - \psi(\tilde{v}, \theta)] H[\tilde{u}(\tilde{v}) - \tilde{u}_0] \frac{1}{\cos \psi(\tilde{v}, \theta)} \tilde{u}(\tilde{v})^{-\gamma-4}, \qquad (36)$$

where the Heaviside step function $H[x]$ ensures proper range of initial velocities and $\tilde{u}_0 = u_0/v_{esc}$. For normal ejecta, when $f_\psi(\psi) = \delta(\psi) = \tilde{u}\delta(\theta)/(\tilde{r}\tilde{v})$, Eq. (35) reads

$$n(\tilde{r}, \tilde{v}, \theta)$$

$$= \frac{N^+}{8\pi^2 r_M^2 v_{esc}^4} \gamma \tilde{u}_0^\gamma H[\tilde{u}(\tilde{v}) - \tilde{u}_0] \frac{\delta(\theta)}{\tilde{r}^2 \tilde{v}^2 \sin \theta} \tilde{u}(\tilde{v})^{-\gamma-2}. \qquad (37)$$

Fig. 4 gives contour plots of the function $n(\tilde{r}, \tilde{v}, \theta)$ for Rhea at two fixed distances from the moon. The hatched area of the (v, θ) plane is unreachable for particles ejected from the surface of the moon, and it is described by two Heaviside functions in Eq. (36). The function $n(\tilde{r}, \tilde{v}, \theta)$ has integrable singularities at the border between the reachable and unreachable area, and the shape of the border represents the main difficulty for calculating the quantities of interest out of the phase space distribution function. Fig. 4 shows, in particular, that: grains with speeds above the escape speed at a given distance can only move at small angles θ (these particles never fall back); the lower the speed, the larger the number of the ejecta on the average—approximately a power law dependence, visible in the logarithmic grey scale used in the plots, etc.

3.3. Number density

The distribution function found in the previous subsection can be used to derive a number of quantities of interest. In this subsection, we calculate the number density of dust. According to (31), the number density at a radial position $r = \tilde{r}r_M$ is given by the integral

$$n(\tilde{r}) = \int_0^\infty \int_0^\pi n(\tilde{r}, \tilde{v}, \theta) 2\pi v_{esc}^3 \tilde{v}^2 \, d\tilde{v} \sin \theta \, d\theta. \qquad (38)$$

We now consider separately the particles that move in elliptic and hyperbolic orbits.

3.3.1. Elliptic orbits

In this case mechanical energy is less than 0, which gives a condition upon the velocity components $(\tilde{v}, \theta)$ depending on a radius $r = \tilde{r}r_M$:

$$\tilde{v} < \tilde{v}_C(\tilde{r}) = \tilde{r}^{-1/2}. \qquad (39)$$

Another condition reflects the fact that a dust particle with phase space coordinates $(\tilde{r}, \tilde{v}, \theta)$ must originate at the surface of the moon. Since transformation (32) is unique, the easiest way to calculate the second condition is to find a range of velocities $(\tilde{v}, \theta)$ at position $\tilde{r}$, for which initial velocity $(\tilde{u}, \psi)$ calculated with Eqs. (33) is real. After simple algebraic manipulations, one gets

$$\theta < \theta_C(\tilde{r}, \tilde{v}) = \begin{cases} \pi/2, & 0 \leqslant \tilde{v} \leqslant \tilde{v}_1, \\ \arcsin[\frac{1}{\tilde{r}\tilde{v}}\sqrt{\tilde{v}^2 + 1 - 1/\tilde{r}}] & \tilde{v}_1 < \tilde{v} < \tilde{v}_C, \end{cases} \qquad (40)$$

where $\tilde{v}_1 = 1/\sqrt{\tilde{r}(\tilde{r} + 1)}$. Besides this range for $(\tilde{v}, \theta)$, there are also particles with $(\tilde{v}, \pi - \theta)$—those returning to the moon. Because of the symmetry, the formula for the phase distribution $n(\tilde{r}, \tilde{v}, \theta)$ is the same as in the first case. The complement of Eqs. (39) and (40), the unreachable velocities, is hatched in Fig. 4.

Taking expression (38) for $\tilde{v} < \tilde{v}_C$ and $\theta < \theta_C$ and integrating over all velocities, we get the number density of dust grains at a position $r = \tilde{r}r_M$:

$$n_{bound}(\tilde{r}) = 2 \int_0^{\tilde{v}_C} \int_0^{\theta_C} n(\tilde{r}, \tilde{v}, \theta) 2\pi v_{esc}^3 \tilde{v}^2 \, d\tilde{v} \sin \theta \, d\theta \qquad (41)$$

with factor 2 in front of the integrals coming from the symmetry of the problem ($\theta \leftrightarrow \pi - \theta$).
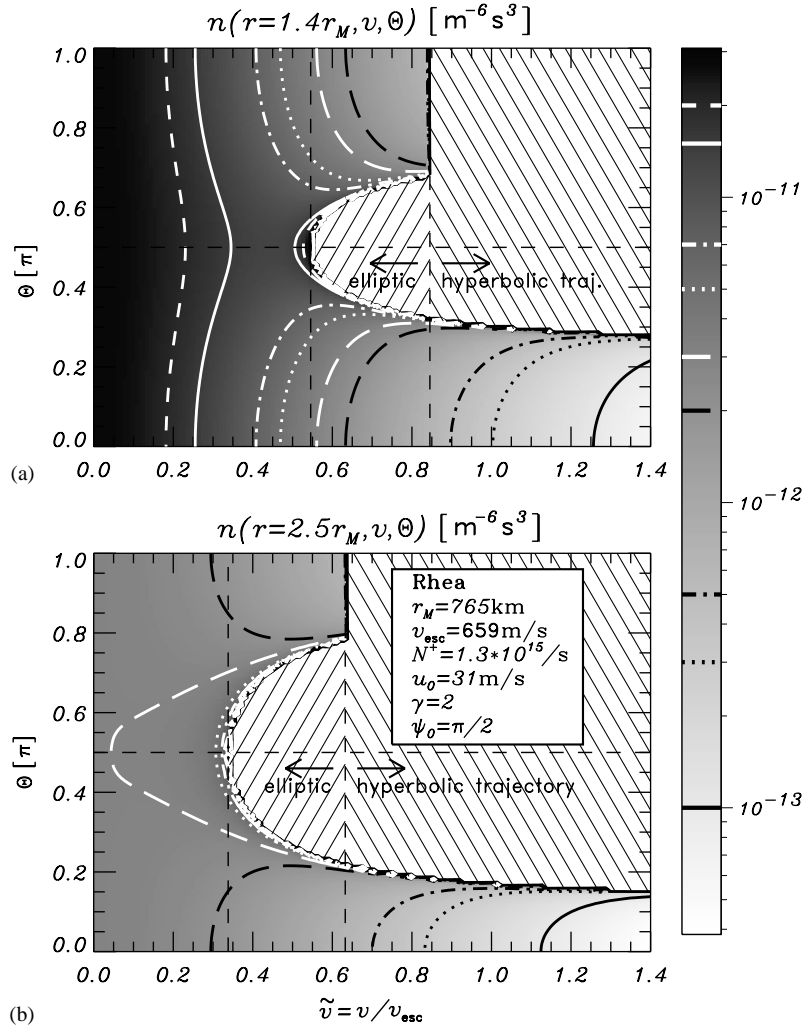
Fig. 4. Two plots of phase distribution function $n(r, v, \theta)$ (a uniform initial distribution of ejection angle, Eq. (36)) for two distances from Rhea. The set of parameters used is written in the plots. The logarithmic grey scale is the same in both panels and includes also isolines of $n(r, v, \theta)$. The hatched area of (v, θ) plane is unreachable for particles ejected from the surface of the moon.

For the initial distributions introduced in Section 2.3, we get the following expression for number density of ejected dust grains into elliptic orbits:

$$n_{\text{bound}}(\tilde{r}) = \frac{N^+}{2\pi r_{\text{M}}^2 v_{\text{esc}}} \gamma \tilde{u}_0^\gamma \tilde{r}^{-5/2} K_{\text{bound}}(\tilde{r}). \tag{42}$$

The form factor $K(\tilde{r})$ weakly depends on distance $\tilde{r}$, tending to unity for large $\tilde{r}$. An explicit expression for K in general case is

$$K_{\text{bound}}^{\psi_0}(\tilde{r})$$
$$= \frac{\tilde{r}^{3/2}}{1 - \cos\psi_0} \left[\frac{1}{2} \int_{\tilde{u}_1}^{\tilde{u}_2} d\tilde{u}\, \tilde{u}^{-\gamma-2} \ln \frac{\tilde{u}/\tilde{r} + \tilde{v}(\tilde{u})}{\tilde{u}/\tilde{r} - \tilde{v}(\tilde{u})} \right.$$
$$\left. + \int_{\tilde{u}_2}^1 d\tilde{u}\, \tilde{u}^{-\gamma-2} \ln \frac{\tilde{v}(\tilde{u}) + \tilde{u}/\tilde{r}}{\sqrt{\tilde{v}^2(\tilde{u}) - \tilde{u}^2 \sin^2\psi_0/\tilde{r}^2 + \tilde{u}\cos\psi_0/\tilde{r}}} \right] \tag{43}$$

and for two limiting cases

$$K_{\text{bound}}^{\psi_0=0}(\tilde{r}) = \tilde{r}^{1/2} \int_{\tilde{u}_1}^1 d\tilde{u}\, \tilde{u}^{-\gamma-1} \frac{1}{\tilde{v}(\tilde{u})} \tag{44}$$

and

$$K_{\text{bound}}^{\psi_0=\pi/2}(\tilde{r}) = \frac{1}{2} \tilde{r}^{3/2} \int_{\tilde{u}_1}^1 d\tilde{u}\, \tilde{u}^{-\gamma-2} \ln \frac{\tilde{v}(\tilde{u}) + \tilde{u}/\tilde{r}}{|\tilde{v}(\tilde{u}) - \tilde{u}/\tilde{r}|}. \tag{45}$$

Limits of the integrals are $\tilde{u}_1 = \max\left\{ \sqrt{(\tilde{r}-1)/\tilde{r}}, \tilde{u}_0 \right\}$ and $\tilde{u}_2^2 = \tilde{r}(\tilde{r}-1)/(\tilde{r}^2 - \sin^2\psi_0)$. In the derivation of the above formulae from Eq. (41), integration over the angles is carried out using the identity

$$\int \frac{\sin\xi\, d\xi}{\sqrt{1 - A^2 \sin^2\xi}} = -\frac{1}{A} \ln\left[A\cos\xi + \sqrt{1 - A^2 \sin^2\xi} \right]. \tag{46}$$

The Heaviside step function $H[\psi_0 - \psi(\tilde{v}, \theta)]$ is resolved in a way similar to Eq. (40). Then, integrals over the final velocities $\tilde{v}$ are transformed to integrals over the initial velocities $\tilde{u}$, using $\tilde{v}(\tilde{u}) = \sqrt{\tilde{u}^2 - 1 + 1/\tilde{r}}$ (Eq. (32)). The limit $\tilde{u}_1$ takes into account the lower limit of the initial velocities $\tilde{u}_0$, and we assumed that $\tilde{u}_0 < 1$. Eq. (44) can be obtained either by inserting the phase space distribution function (37) into Eq. (41), when integral over the angles θ is trivial because of the presence of the Dirac delta function, or by taking the limit $\psi_0 \to 0$ of Eq. (43). The result, Eq. (44), was already found by Krüger et al. (2000), and presented in a form of the integral over $\xi = \tilde{r}^{-1}(1 - \tilde{u}^2)^{-1}$.

For large distances, in practice $\tilde{r} > 2$, the lower limit is $\tilde{u}_1 = \sqrt{(\tilde{r} - 1)/\tilde{r}}$. Then, using the substitution $\xi = \tilde{r}^{-1}(1 - \tilde{u}^2)^{-1}$ the expression for the form factor for the normal ejecta case can be written in a closed analytic form

$$K_{\text{bound}}^{\psi_0=0}(\tilde{r}) = F\left[1, 1 + \frac{\gamma}{2}; \frac{3}{2}; \frac{1}{\tilde{r}}\right], \qquad (47)$$

where $F[a, b; c; d]$ is a hypergeometric function (Abramowitz and Stegun, 1970), given by the following equivalent definitions:

$$F[a, b; c; z]$$

$$\equiv F[b, a; c; z] \equiv \frac{\Gamma[c]}{\Gamma[a]\Gamma[b]} \sum_{n=0}^{\infty} \frac{\Gamma[a + n]\Gamma[b + n]}{\Gamma[c + n]} \frac{z^n}{n!}$$

$$\equiv \frac{\Gamma[c]}{\Gamma[b]\Gamma[c - b]} \int_0^1 dt\, t^{b-1}(1 - t)^{c-b-1}(1 - tz)^{-a}, \quad (48)$$

where $\Gamma[\xi] = (\xi - 1)\Gamma[\xi - 1]$ is the Gamma function. The asymptotic limit $r \to \infty$ for the form factors in two limiting cases is

$$K_{\text{bound}}^{\psi_0=0}(\tilde{r})$$

$$= 1 + \frac{\gamma + 2}{3}\frac{1}{\tilde{r}} + \frac{(\gamma + 2)(\gamma + 4)}{15}\frac{1}{\tilde{r}^2} + O[\tilde{r}^{-3}], \qquad (49)$$

$$K_{\text{bound}}^{\psi_0=\pi/2}(\tilde{r}) = 1 + \frac{\gamma + 1}{3}\frac{1}{\tilde{r}} + \frac{\gamma^2 + \gamma + 7}{15}\frac{1}{\tilde{r}^2} + O[\tilde{r}^{-3}]. \quad (50)$$

Expression (49) is a straightforward consequence of Eqs. (47) and (48), while Eq. (50) can be obtained for instance by considering Eq. (45) in two intervals and applying substitutions $\xi^2 = 1/(1 - \tilde{u}^2) - \tilde{r}$ on $\tilde{u} \in [\tilde{u}_1, \tilde{u}_2]$ and $\xi = (\tilde{u}^{-2} - 1)\tilde{r}$ on $\tilde{u} \in [\tilde{u}_2, 1]$.

The form factor K_{bound} is depicted in Fig. 5. It is always bigger than 1, but approximately after $\tilde{r} > 10$ it becomes less than 1.1—the correction to a $\tilde{r}^{-5/2}$ dependence of the number density is less than 10%. Series expansions (49) and (50) can be used when $\tilde{r} > 2$, approximately, but in the inner region the radial dependence of the number density deviates from $\tilde{r}^{-5/2}$ markedly ($K_{\text{bound}} > 1$), and one must use the explicit expressions for K_{bound}. The increase of the opening angle ψ_0 decreases K_{bound} and the number density. The dependence of K_{bound} on ψ_0 is smooth and monotonous,
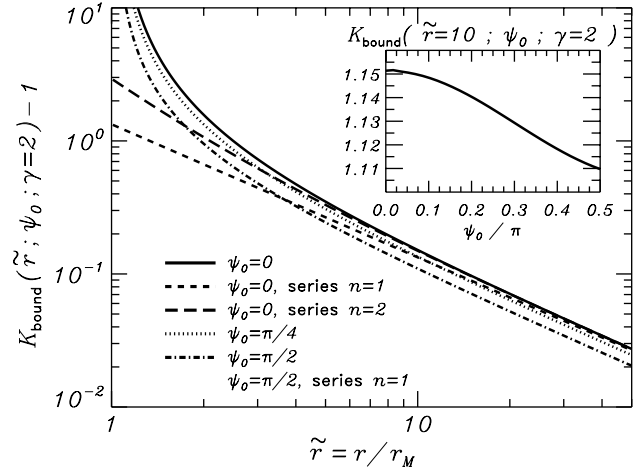

Fig. 5. Dependence of the form factor K_{bound} on the scaled radius $\tilde{r}$ for different opening angles ψ_0 (Eq. (43)). Series expansions are also plotted, meaning that $n = 1$ is an expansion up to $\tilde{r}^{-1}$. Inset: Dependence of K_{bound} on the opening angle ψ_0 for fixed radius $\tilde{r} = 10$. The coefficient γ was taken to be $\gamma = 2$.

and $\psi_0 = 0$ and $\pi/2$ represent two limiting cases. In the region where series expansions (49) and (50) work ($\tilde{r} > 2$), the opening angle dependence is quite small, but in the inner region it can become much larger.

3.3.2. Hyperbolic orbits

Here we apply the same procedure as for elliptic orbits, and therefore do not discuss it in detail. Conditions upon the velocity coordinates $(\tilde{v}, \theta)$ are now

$$\tilde{v} > \tilde{v}_C(\tilde{r}) = \tilde{r}^{-1/2}, \theta < \theta_C = \arcsin\left[\frac{1}{\tilde{r}\tilde{v}}\sqrt{\tilde{v}^2 + 1 - 1/\tilde{r}}\right], \qquad (51)$$

but this time without the symmetric case, since particles are not bouncing back to the moon from the infinity. The number density is expressed as

$$n_{\text{unbound}}(\tilde{r}) = \int_{\tilde{v}_C}^{\infty} \int_0^{\theta_C} n(\tilde{r}, \tilde{v}, \theta) 2\pi v_{\text{esc}}^3 \tilde{v}^2 \, d\tilde{v} \sin\theta \, d\theta. \quad (52)$$

The result of the double integration is

$$n_{\text{unbound}}(\tilde{r}) = \frac{N^+}{4\pi r_M^2 v_{\text{esc}}} \gamma \tilde{u}_0^\gamma \tilde{r}^{-2} c_0(\gamma) K_{\text{unbound}}(\tilde{r}), \qquad (53)$$

where $K_{\text{unbound}}(\tilde{r})$ is again a form factor, weakly depending on distance and tending to unity for large $\tilde{r}$, and

$$c_0(\gamma) = \frac{\sqrt{\pi}\Gamma[(\gamma + 1)/2]}{\gamma\Gamma[\gamma/2]} \qquad (54)$$

is a monotonically decaying function of γ : $c_0(1) = 1, c_0(2) = \pi/4, c_0(3) = 2/3$, etc. The explicit expression for K, written

as an integral over the initial velocities $\tilde{u}$, is

$$
K_{\text{unbound}}^{\psi_0}(\tilde{r}) = \frac{\tilde{r}}{(1 - \cos\psi_0)c_0(\gamma)}
$$
$$
\times \int_1^\infty d\tilde{u}\,\tilde{u}^{-\gamma-2}\ln\frac{\tilde{v}(\tilde{u}) + \tilde{u}/\tilde{r}}{\sqrt{\tilde{v}^2(\tilde{u}) - \tilde{u}^2\sin^2\psi_0/\tilde{r}^2} + \tilde{u}\cos\psi_0/\tilde{r}}
$$
(55)

and for two limiting cases

$$
K_{\text{unbound}}^{\psi_0=0}(\tilde{r}) = \frac{1}{c_0(\gamma)}\int_1^\infty d\tilde{u}\,\tilde{u}^{-\gamma-1}\frac{1}{\tilde{v}(\tilde{u})},
$$
(56)

$$
K_{\text{unbound}}^{\psi_0=\pi/2}(\tilde{r}) = \frac{\tilde{r}}{2c_0(\gamma)}\int_1^\infty d\tilde{u}\,\tilde{u}^{-\gamma-2}\ln\frac{\tilde{v}(\tilde{u}) + \tilde{u}/\tilde{r}}{\tilde{v}(\tilde{u}) - \tilde{u}/\tilde{r}}.
$$
(57)

Again, integration over the angles is carried out using Eq. (46), and integrals over the final velocities $\tilde{v}$ are transformed to integrals over the initial velocities $\tilde{u}$. Eq. (56) is a $\psi_0 \to 0$ limit of Eq. (55), or a result of the direct integration of the phase space distribution function (37), and it was already found by Krüger et al. (2000). Further, making the substitution $\xi = \tilde{u}^{-2}$ and applying linear transformation formulae for the hypergeometric function F (Abramowitz and Stegun, 1970), the result is

$$
K_{\text{unbound}}^{\psi_0=0}(\tilde{r}) = \left(1 - \frac{1}{\tilde{r}}\right)^{-(1+\gamma)/2}
$$
$$
- \frac{1}{\sqrt{\tilde{r}}c_0(\gamma)}F\left[1, 1 + \frac{\gamma}{2}; \frac{3}{2}; \frac{1}{\tilde{r}}\right].
$$
(58)

Series expansions valid for large distances $\tilde{r}$ are

$$
K_{\text{unbound}}^{\psi_0=0}(\tilde{r}) = 1 - \frac{1}{c_0(\gamma)}\tilde{r}^{-1/2} + \frac{\gamma+1}{2}\tilde{r}^{-1} - \frac{\gamma+2}{3c_0(\gamma)}\tilde{r}^{-3/2}
$$
$$
+ \frac{(\gamma+1)(\gamma+3)}{8}\tilde{r}^{-2} + \mathrm{O}[\tilde{r}^{-5/2}],
$$
(59)

$$
K_{\text{unbound}}^{\psi_0=\pi/2}(\tilde{r}) = 1 - \frac{1}{c_0(\gamma)}\tilde{r}^{-1/2} + \frac{\gamma+1}{2}\tilde{r}^{-1} - \frac{\gamma+1}{3c_0(\gamma)}\tilde{r}^{-3/2}
$$
$$
+ \frac{9 + 4\gamma + 3\gamma^2}{24}\tilde{r}^{-2} + \mathrm{O}[\tilde{r}^{-5/2}].
$$
(60)

Eq. (59) can be obtained from Eq. (58), and Eq. (57) after the substitution $\xi = \tilde{u}^{-2}$ leads to Eq. (60). The resulting expansions show quite different behavior from the case of elliptic orbits. First we notice that the difference between the two limiting cases for the opening angle ψ_0 is small— the first three terms in the expansions are the same. On the other hand, K_{unbound} is not as close to unity as K_{bound}, since the leading term in the expansions is $\propto \tilde{r}^{-1/2}$.

The form factor K_{unbound} is plotted in Fig. 6. As we expected from series expansions, the dependence on the opening angle ψ_0 is weak, and K_{unbound} increases monotonically with ψ_0. The factor deviates from unity by less than 10% for $\tilde{r} > 100$, as one can expect from Eqs. (59) and (60), and the series remain in force for $\tilde{r} > 5$. In the inner region the dependence on ψ_0 becomes perceptible, giving $K_{\text{unbound}} < 1$ for small ψ_0 and $K_{\text{unbound}} > 1$ for ψ_0 near $\pi/2$.
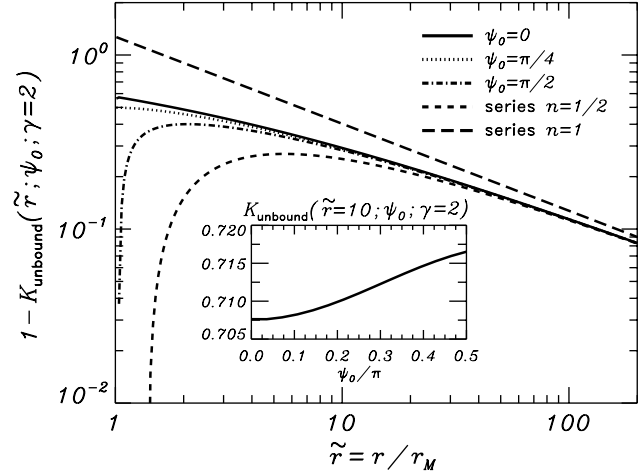

Fig. 6. The form factor K_{unbound}. Notation is the same as in Fig. 5. The first three terms in the series expansions are the same ($n = 1/2$ means an expansion up to $\tilde{r}^{-1/2}$). The form factor K_{unbound} for $\psi_0 = \pi/2$ close to the moon exceeds unity and is diverging as $\tilde{r} \to 1$, as series expansions are not valid in the region close to the surface.

3.4. Summary

In the second part of the model, we found a closed analytic expression (Eq. (35)) for a phase space (space–velocity) distribution function, which contains full information about the dust cloud around a spherically symmetric parent body. This result is valid for any mechanism of dust production. The only assumptions are uniform dust production from the surface and Keplerian dynamics of the ejected particles. Number densities, velocity distributions, dust fluxes and other quantities of interest can be calculated as integrals of this distribution function.

In particular, we derived the number density of dust at a given distance r from a satellite: $n(r) = n_{\text{bound}}(r) + n_{\text{unbound}}(r)$, where contributions of grains in elliptic and hyperbolic orbits are given by Eqs. (42) and (53), respectively. These expressions contain, as a factor, the dust production rate from the satellite surface N^+, which can be computed with the aid of Eqs. (10) and (11). They also contain form factors, K_{bound} in the first case and $c_0 K_{\text{unbound}}$ in the second, which weakly depend on r, speed distribution slope γ, as well as the angular distribution of ejecta velocities at the surface. For the sake of estimates one can safely replace the form factors with unity. If more accurate calculations are required, the form factors can be calculated either with closed-form expressions in special functions (Eqs. (47), (54) and (58)) or with series expansions (Eqs. (49), (50), (59) and (60)).

Some properties of the radial distribution of the number density were discussed earlier in Krüger et al. (2000). One of them is that, at a given scaled distance $\tilde{r}$, the density is lower for larger satellites: Eqs. (42) and (53) give the scaling $n \propto r_{\text{M}}^{-\gamma-1}$. Another finding is that the number density in a cloud scales with the distance approximately as $r^{-2.5}$ for
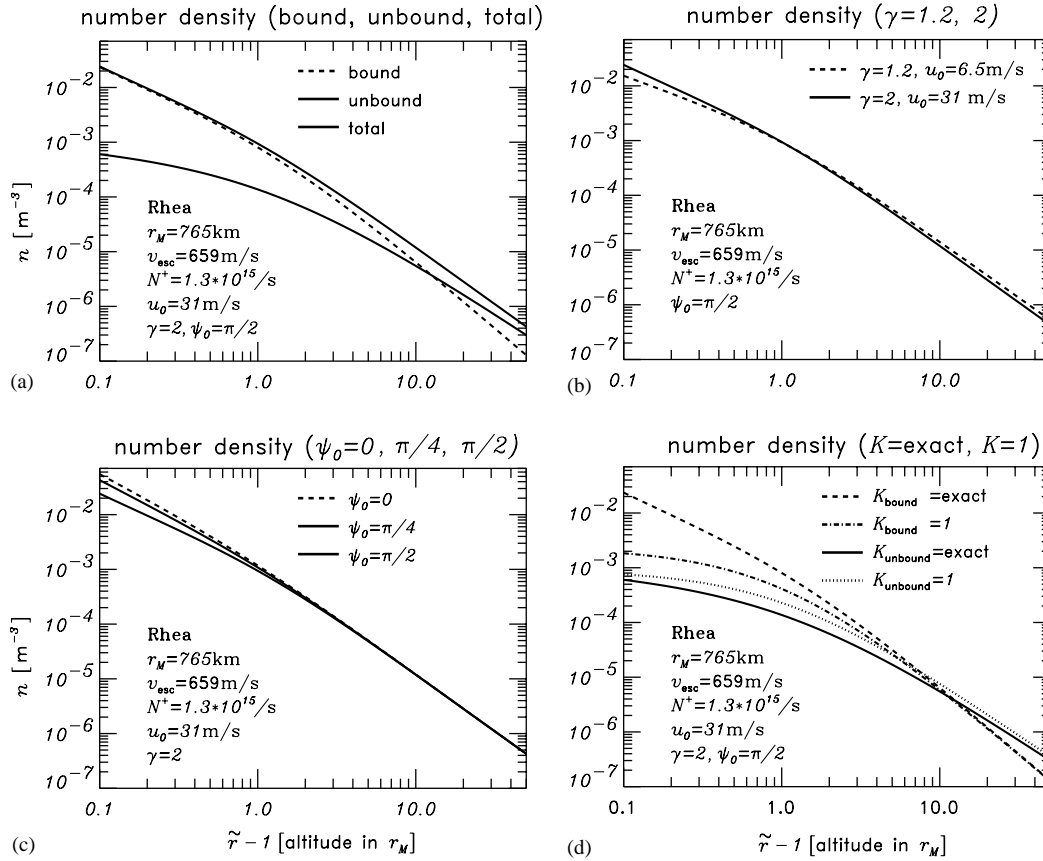
Fig. 7. Number density vs. altitude above the satellite surface calculated for Rhea. Panels show relative contributions of grains in ballistic and escaping trajectories (a) as well as influence of different parameters on the results: slope of the ejecta speed distribution (b), opening angle of the ejecta cone (c), form factors K (d). In panel (b), we use different values of u_0 for different γ in accordance with Eqs. (19) and (20).

bound and r^{-2} for unbound grains. Yet another result is that, surprisingly enough, the difference between the two limiting cases of the angular velocity distribution is very small. In other words, the number density profile depends only weakly on the angular distribution of the ejecta from the surface of a moon.

These properties are illustrated in Fig. 7 that depicts the number density of the dust cloud of Rhea as a function of distance from the satellite surface. In panel (a), we show separately the contributions made to the number density by the particles in ballistic (bound) and unbound trajectories and their sum. Panels (b)–(d) depict the results for different choices of several model parameters, showing a surprisingly weak dependence of the dust density on these parameters at several moon's radii from the surface.

4. Number density of dust

4.1. Dust at Ganymede: Galileo DDS measurements

Fig. 8 plots the number density derived from the Galileo DDS data, obtained during two of its four flybys of Ganymede, G1 and G7 (symbols with error bars). These

two flybys are chosen because they brought the most reliable data in contrast to the G2 and G8 data which were processed with large correction factors for incomplete data transmission (Krüger et al., 1999, 2000). Detailed information of the Galileo measurements at Ganymede, as well as full description of the data and their processing can be found in our previous papers (Krüger et al., 1999, 2000). An important point to be made here is that the derivation of the number density from the Galileo data assumed a constant effective sensitive area of the detector (calculated individually for each of the Galileo flybys of Ganymede). It means that the real detector, spinning with the spacecraft around an axis pointing in the anti-Earth direction, was effectively replaced with a hypothetical detector with a smaller sensitive area, constantly looking in the ram direction of the spacecraft. Such an assumption is generally not valid for Cassini CDA, which is not in a passive rotation and the articulation of which is controlled manually. We will discuss this later.

In the same figure, we plotted the number density of the dust cloud, calculated with the model (Section 3). Fig. 8 shows a reasonably good agreement between the model and the measurement results. We note that the number densities given by the present model are close to those provided by a cruder model used before (Krüger et al., 2000), which
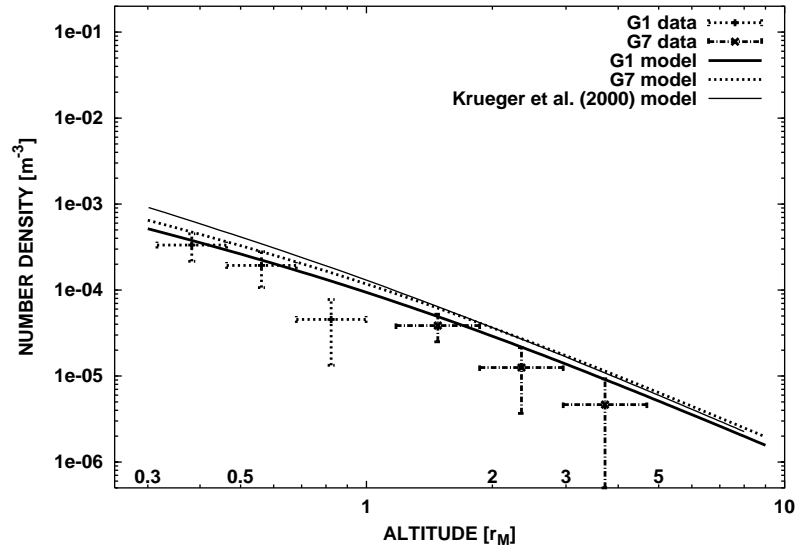
Fig. 8. Number density of the dust cloud around Ganymede. Symbols with error bars: number density derived from the Galileo measurements during its G1 and G7 flybys. Thick lines: number density in the dust cloud around Ganymede in case of uniform (isotropic) distribution. In these calculations, we assumed model parameters from Tables 2 and 3. Note that the model curves for the two flybys are slightly different, because so are the flyby velocity and therefore the minimum mass of the detected grains. Thin solid line: model calculations of Krüger et al. (2000) who assumed a normal ejection from the surface and a slightly different set of model parameters: $Y = 10^4, u_0 = 30$ m s$^{-1}, \gamma = 1.6, \alpha = 0.83, M_{max} = 10^{-5}$ g, $M_{min} = 10^{-13}$ g.
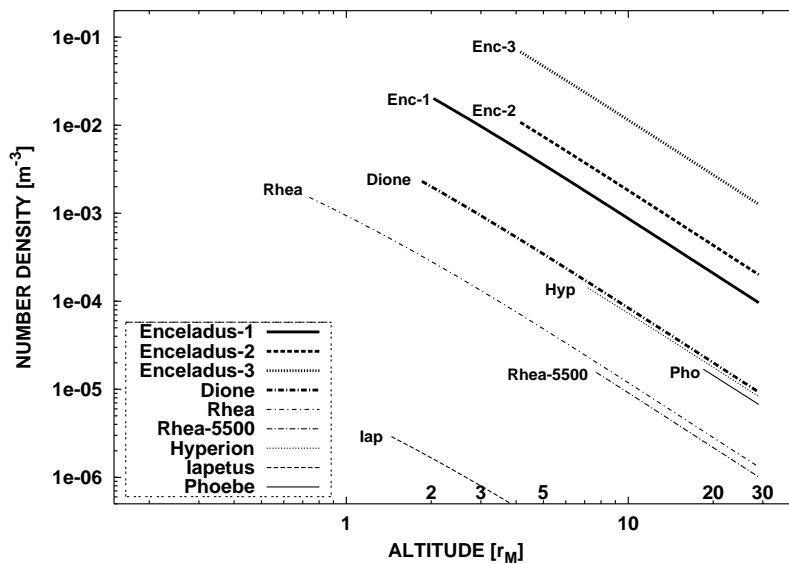

Fig. 9. Number density of the dust clouds around six saturnian satellites (uniform initial angular distribution of ejecta assumed). Distance from each moon is scaled with a moon radius. Different model curves for the different flybys of one and the same satellite (Enceladus, Rhea) appear, because the flyby velocity and therefore the estimated CDA threshold are different. Each curve is cut at the C/A altitude.

assumed a normal ejection of dust from the surface. A detailed comparison between the model and Galileo data, given in that paper, applies to the present model. Any tangible improvement of the poorly known parameters (yield, slope of the ejecta speed distribution, etc.) is unfortunately not possible, because of the scarcity of the data, especially at small and large altitudes. We can only state that the parameters chosen are compatible with the data.

4.2. Dust at saturnian moons: Cassini CDA measurements

Similar to Fig. 8 for Ganymede, Fig. 9 plots the number density of the dust clouds around all six saturnian satellites of interest (uniform ejection only). Both figures have the same vertical scale, enabling immediate visual comparison of the number densities in both cases. The max-

Table 4
Satellite flybys and expected maximum number densities and impact rates at C/A. The last column gives the expected cumulative number of impacts during a flyby

Satellite and flyby	Distance (r_M)	Enc. speed (km s^{-1})	Mass threshold (g)	Num. dens. (m^{-3})	Imp. rate (min^{-1})	Total number of impacts
Enceladus1	3.0	6.4	6.0×10^{-14}	2.0×10^{-2}	600[a]	3600[a]
Enceladus2	5.0	8.1	2.4×10^{-14}	1.2×10^{-2}	500[a]	3400[a]
Enceladus3	5.0	14.6	2.4×10^{-15}	7.3×10^{-2}	5000[a]	20000[a]
Dione	2.8	9.0	1.6×10^{-14}	2.5×10^{-3}	100	800
Rhea	1.7	7.3	3.6×10^{-14}	1.7×10^{-3}	60	400
Rhea-5500	8.5	6.7	5.0×10^{-14}	1.6×10^{-5}	0.5	18
Hyperion	8.0	5.6	1.0×10^{-13}	1.5×10^{-4}	4[b]	40[b]
Iapetus	2.4	2.4	2.8×10^{-12}	3.1×10^{-6}	0.04	0.9
Phoebe	19.2	6.4	6.0×10^{-14}	1.7×10^{-5}	0.5	9

[a] Will be higher if E-ring projectiles are important.
[b] Will be higher if Phoebe projectiles and/or those from recently discovered outer retrograde moons are important.

imum expected number densities of the actual Cassini flybys (Table 4) range from $\sim 10^{-5}$ m^{-3} (Iapetus) to $\sim 10^{-1}$ m^{-3} (Enceladus-3). For comparison, the values derived from the Galileo dust detector data obtained during its flybys of the Galilean moons of Jupiter and explained with a model similar to the one considered here (Krüger et al., 1999, 2000) were about 10^{-5}–10^{-3} m^{-3}. That the typical densities in Fig. 8 (Jupiter) are lower than in Fig. 9 (Saturn) is understandable. As was shown in Section 3.4, the number density at the same distance (measured in the satellite radii) for larger moons (Ganymede) is lower than for smaller ones (the saturnian moons considered here).

5. Velocities of dust grains, detector pointing, and impact rates

5.1. Maximum impact rates

A strict way to find fluxes on CDA, as well as to study their dependence on the CDA orientation, is to integrate the effective sensitive area of the detector, multiplied by the predicted speed of the dust grains and by the phase distribution function $n(r, v, \theta)$. Before we proceed with these calculations, let us estimate expected maximum impact rates on Cassini CDA. Effects of different possible orientations of the detector will be considered later. Here, we assume that CDA points to the ram direction which, as we shall see below, maximizes the impact rates. Therefore, the effective sensitive area is taken to be ~ 800 cm^2 (impact ionization target, see Srama et al., 2002). We have an expression for the impact rate

$$\frac{I}{\min^{-1}} \approx 4800 \left(\frac{n}{1\ m^{-3}}\right) \left(\frac{v}{1\ km\ s^{-1}}\right). \quad (61)$$

Numerical results are depicted in Table 4, showing that a mean impact rate is, in most of the cases, greater (sometimes by far) than the impact rate on the Galileo dust detector during its flybys of the Galilean moons, ~ 1 min^{-1} (Krüger et al., 1999, 2000). Also calculated is the total number of

impacts for each of the flybys, which is the impact rate integrated along the spacecraft trajectory.

Remember that the number densities, impact rates, and total numbers of impacts in Table 4 are given for particles with masses above the CDA threshold for actual encounter speeds of Cassini. This explains, for instance, a large difference between the flybys of Enceladus: the larger the flyby speed, the lower the mass threshold, and the higher the number density.

Another striking difference is the one between the impact rates near inner and outer satellites—e.g., Enceladus-1 and Phoebe flybys. This three-order-of-magnitude difference comes from: (i) the gravitational focusing of impactors by Saturn's gravity, which is much stronger at Enceladus, (ii) different surface properties of these moons—Enceladus' surface should give higher yield as Phoebe's, and (iii) a much smaller flyby distance for Enceladus-1.

High impact rates at Enceladus, hundreds to thousands of hits per minute, should be compared to the E-ring background. Tsintikidis et al. (1995) (see also Meyer-Vernet et al., 1996) indicate the impact rate of (probably) micron-sized particles on Voyager spacecraft near Dione orbit of about 50 m^{-2} s^{-1}. Correcting for different speeds of Cassini and Voyager (9 vs. 18 km s^{-1}) and for the CDA area (0.08 m^2), we get the background impact rate on CDA of about 120 min^{-1}. This is comparable to the impact rate of the Dione cloud particles!

Another estimate can be made as follows. At Enceladus, assume the vertical thickness of the E ring of 10^4 km, and a column density of μm-sized particles of $\sim 10^2$ cm^{-2} (e.g., Spahn et al., 1999). Then the mean number density is ~ 0.1 m^{-3}. This is again comparable to, if not larger than, the predicted number densities at distances of closest approach (C/A) with Enceladus which, by the way, correspond to somewhat smaller grains. Furthermore, a recent E-ring model by Juhász and Horányi (2002) suggests yet larger number density of 1-μm-sized grains in the densest part of the ring, about several particles per m^{-3} (see their Fig. 5). On the other hand, we should note that the size distributions

Table 5
Speed distribution of grains in the circumsatellite clouds

Satellite	$r[r_M]$	Fraction (%) of grains that reach r	Of these, fraction (%) of grains faster than			
			100 m s^{-1}	200 m s^{-1}	500 m s^{-1}	1000 m s^{-1}
Enceladus	3.0	3	72	40	9	2
	5.0	3	76	44	11	3
Dione	3.0	0.6	94	81	40	14
Rhea	2.0	0.4	96	84	46	17
Hyperion	8.0	33	69	39	13	5
Iapetus	2.0	6	96	86	52	24
Phoebe	19.0	69	50	25	9	3

and impact velocities of the E-ring grains and Enceladus cloud particles are likely to be quite different, which makes a quantitative comparison of the cloud and background grains hardly possible.

Predictions for Enceladus could also be checked against some results obtained earlier in an attempt to improve the E-ring models. Dikarev (1999) showed that the vertically integrated edge-on optical depth of the E-ring derived from the observations (Showalter et al., 1991) is consistent with the E-ring dynamical models that use the interplanetary impactor model of Grün et al. (1985) for the model parameters $\alpha = 0.8$ and $Y\eta \sim 10^4$ (η is the fraction of grains escaping from Enceladus). With the mass flux used here, which is almost larger by two orders of magnitude (see Section 2.1), the best-fit $Y\eta$ is $\sim 10^2$. In our model, the actual values are $Y \sim 2 \times 10^4$ and $\eta \equiv (v_{esc}/u_0)^{-\gamma} \sim 10^{-2}$, so that $Y\eta$ is indeed close to $\sim 10^2$.

5.2. Dispersion of grain velocities

We now make simple estimates of the velocity dispersion of the dust grains at a given distance from a given satellite. The speed distribution at the surface $f_u(u)$ is given by Eq. (17). Considering, as earlier, the motion of grains in Keplerian trajectories and applying the energy integral, we obtain a distribution of speed v at a distance r from the satellite:

$$g_v(r,v) = f_u(u)v/u, \qquad (62)$$

where u should be expressed through v with the aid of the formula

$$u = \sqrt{v^2 + v_{esc}^2(1 - r_M/r)}. \qquad (63)$$

Denote by

$$G(r, > v) = \int_v^{+\infty} g_v(r,v)\,dv \qquad (64)$$

the fraction of ejecta that reach the distance r at speeds $> v$. This function is normalized in such a way that $G(r, > 0)$ is a fraction of the ejecta that are fast enough to reach the distance r. The values of the function $G(r, > 0)$ are listed in Table 5 for all satellites of interest, where r is a flyby distance. Also listed are the ratios $G(r, > v)/G(r, > 0)$ for

several values of speed v. These ratios give us a fraction of the grains faster than v among all the grains at a distance r.

For small satellites (Hyperion, Phoebe), the fraction of grains that reach the flyby distance is relatively large (tens of percent), but their rest velocities are small (about 90% of the particles have speeds less than 500 m s^{-1}). Large satellites (Dione, Rhea, Iapetus) show the opposite: less than 1% of the ejecta reach substantial altitudes above the surface, but those that reach them have a tangible velocity dispersion: about 40–50% of them have a speed greater than 500 m s^{-1}.

These results allow us to estimate the pointing requirements for the Cassini CDA during the satellite flybys. To maximize the impact rates, CDA should be directed close to the apex of the Cassini motion with respect to the satellite. Maximum deviation of the optimum CDA axis direction from the apex can be estimated as v_{dust}/v_{flyby} rad, where v_{dust} is the typical velocity of dust grains in a cloud estimated above and v_{flyby} in the Cassini speed, both with respect to the moon. For instance, for the Hyperion flyby (see Table 5) $\approx 90\%$ of dust will have velocities $v_{dust} < 500$ m s^{-1} and $v_{flyby} \approx 5.6$ km s^{-1}, so that $\approx 90\%$ of dust will come from within $\approx 0.5/5.6$ rad $\approx 5°$ from the apex.

Using the fact that dust is concentrated around the apex, we can also estimate how the impact rate would decrease if the CDA axis had a given offset angle from the apex direction. This is determined by the angular sensitivity of CDA. For example, at an offset angle of 25° the impact rate drops by a factor of 2. If the offset exceeds about 45°, the impact rate reduces to nearly zero—dust cannot be detected anymore.

5.3. Detector pointing and dust fluxes

Like the number density of dust, the flux on CDA can be expressed as an integral of the phase distribution function $n(\vec{r}, \vec{v}) \equiv n(r, v, \theta)$ defined by Eq. (23) and given by Eq. (35). We have

$$F(\vec{r}, \vec{v}_{cas}, \vec{p}_{CDA}) = \int\int\int n(\vec{r}, \vec{v})|\vec{v} - \vec{v}_{cas}|$$
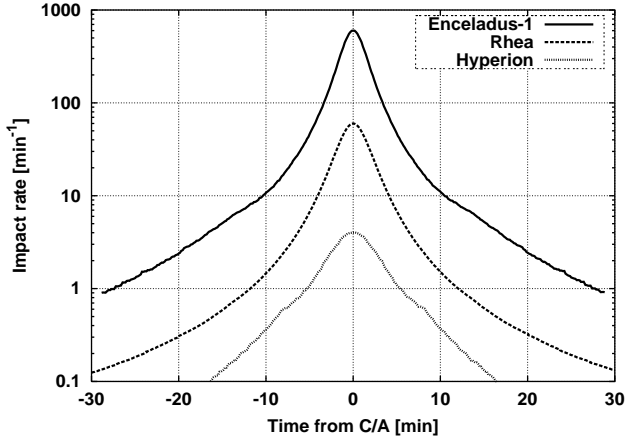$$\times S(\vec{v} - \vec{v}_{cas}, \vec{p}_{CDA})\,d^3\vec{v}, \qquad (65)$$

Fig. 10. Impact rate as function of time for several flybys. The peak is at C/A.

where $\vec{v}_{\mathrm{cas}}$ is the velocity of Cassini relative to the satellite, $S(\vec{v} - \vec{v}_{\mathrm{cas}}, \vec{p}_{\mathrm{CDA}})$ is the effective sensitive area of CDA for dust particles with velocity $\vec{v} - \vec{v}_{\mathrm{cas}}$ with respect to the moon, and a unit vector $\vec{p}_{\mathrm{CDA}}$ is the detector's axis direction. For the effective sensitive area of CDA (impact ionization target), we use a simple approximation (Srama et al., 2002)

$$S(\vec{v} - \vec{v}_{\mathrm{cas}}, \vec{p}_{\mathrm{CDA}}) = 800 \text{ cm}^2 \left[1 - \frac{\angle(\vec{v} - \vec{v}_{\mathrm{cas}}, \vec{p}_{\mathrm{CDA}})}{45°} \right]. \tag{66}$$

Eq. (65) can be rewritten in the form

$$F(r, \vec{v}_{\mathrm{cas}}, \vec{p}_{\mathrm{CDA}})$$
$$= \int_{(v)} \int_{(\theta)} n(r, v, \theta) \Lambda(v, \theta; \vec{v}_{\mathrm{cas}}, \vec{p}_{\mathrm{CDA}}) v^2 \sin\theta \, dv \, d\theta \tag{67}$$

with

$$\Lambda(v, \theta; \vec{v}_{\mathrm{cas}}, \vec{p}_{\mathrm{CDA}})$$
$$\equiv \int_0^{2\pi} |\vec{v}(v, \theta, \lambda) - \vec{v}_{\mathrm{cas}}| S[\vec{v}(v, \theta, \lambda) - \vec{v}_{\mathrm{cas}}, \vec{p}_{\mathrm{CDA}}] \, d\lambda, \tag{68}$$

suitable for numerical evaluation.

Integrals (67) and (68) were evaluated numerically, and the results are depicted in Figs. 10 and 11. Fig. 10 assumes that CDA looks in the ram direction and plots impact rates along the Cassini trajectory as a function of time from C/A. The impact rate drops rapidly with increasing distance from the satellite, because so does the number density in a cloud (close to $\propto r^{-2.5}$, Eq. (42)). For instance, the impact rate at C/A with Rhea, $\sim 60 \text{ min}^{-1}$, reduces to $\sim 7 \text{ min}^{-1}$ five minutes before or after C/A. For small satellites, the impact rate drops even faster. For example, for the Enceladus-1 flyby, the impact rate reduces from ~ 600 to 40 min^{-1} at ± 5 min from C/A. Therefore, measurements beyond several minutes from C/A would already be useless, except for the Enceladus flybys. For Enceladus, the "time window" around C/A may be $\sim \pm 20$ min.
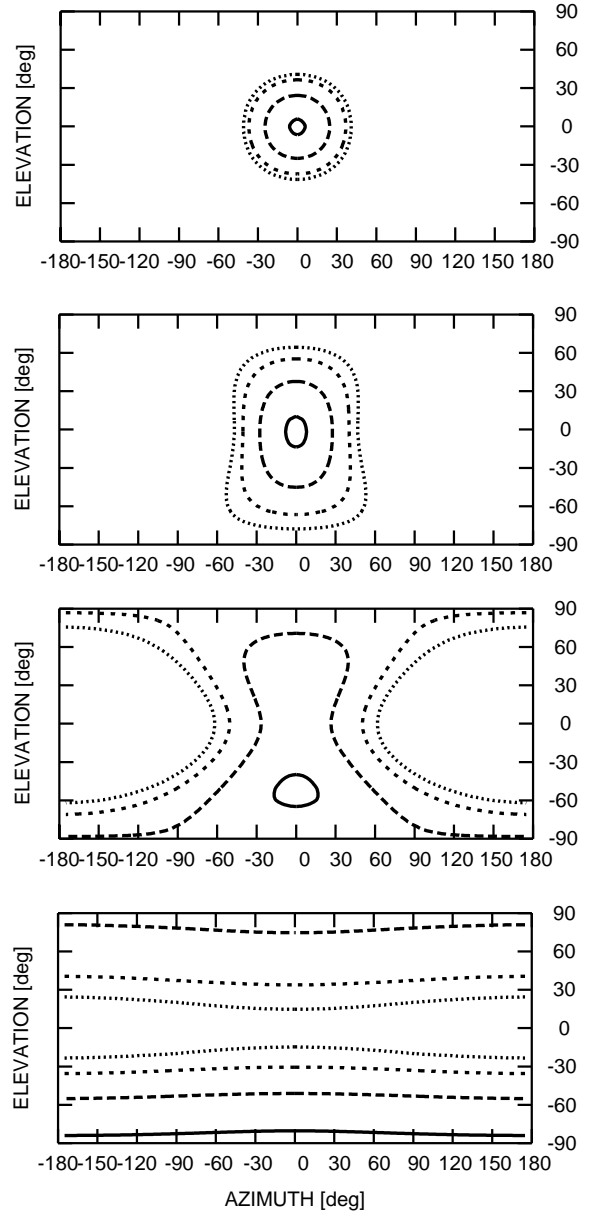

Fig. 11. Predicted impact rate on CDA as a function of its pointing direction for the flyby of Rhea. Panels from top to bottom are for different flyby speeds: 7.3 km s^{-1} (the one actually planned), 0.5 km s^{-1}, 0.2 m s^{-1}, and ≈ 0 m s^{-1}. Each panel maps the "celestial sphere" of Cassini at C/A; the ram direction is at the center and the direction toward the satellite is at the lowest edge of the panel. Isolines show the CDA pointing directions, for which the fluxes are 0.95 (solid), 0.5 (long-dashed), 0.2 (short-dashed), and 0.1 (dotted) times the maximum possible value.

Fig. 11 illustrates the dependence of the impact rates at C/A on the CDA orientation. Each panel represents a distribution of the dust flux on the "celestial sphere" of Cassini. Considering the anti-satellite direction as a pole of this sphere, we introduce usual spherical coordinates—elevation and azimuth. The apex of the Cassini motion, or ram direction, corresponds to elevation and azimuth of zero and is at the center of each panel. The direction to the satellite has the elevation of $-90°$ (azimuth is undefined) and is always

located at the lower border of the panels. At each point, the value plotted is the flux that would be measured by CDA, if its symmetry axis were looking at this point.

As an example, we choose Rhea. The uppermost panel in Fig. 11 shows what would be measured for the planned main flyby of Rhea, with the flyby speed of 7.3 km s^{-1}. The other panels depict the same, but with the Cassini flyby speed being artificially decreased to the values 500, 200 and 10 m s^{-1}. In agreement with simple estimates made above, the plot for the real flyby shows a strong concentration of the flux towards the apex. The isolines of flux are highly symmetric with respect to the apex direction. For lower flyby speeds (or the same speed for larger moons) the central peak, as well as the whole "dust spot" somewhat broaden, and a slight asymmetry of the isolines appears, so that more dust can be detected if CDA looks towards the moon than if it is directed outwards. The less the flyby speed, or the larger the moons, the more pronounced the asymmetry. This is illustrated by lower panels: a substantial asymmetry for $v_{\text{flyby}} \approx 0.2$ km s^{-1} and a limiting case of a "levitating" spacecraft ($v_{\text{flyby}} \approx 0$ km s^{-1}), when much of the material comes from the satellite, although even detections in the anti-satellite direction are possible (grains in ballistic orbits falling back to the moon). It should be stressed that the lower-speed cases, especially the "levitating" one, are purely hypothetical and are considered only to illustrate the dependence of the model fluxes on the detector motion. These cases do not have physical relevance: e.g., the impact ionization process for a dust instrument will not work at very low impact speeds.

6. Summary and conclusions

6.1. Model

In this paper, a model of an impact-generated, steady-state, spherically symmetric dust cloud around an atmosphereless planetary satellite or planet (Mercury, Pluto) is constructed:

(i) The model consists of two parts. First, assuming the projectiles to be interplanetary micrometeoroids, we suggest a simple algorithm of calculating the production rate of ejecta from the surface of the body (Eqs. (10) and (11)). A uniform ejection of dust from the surface is postulated. The ejecta mass and velocity distributions are taken to be power laws, the parameters of which are chosen in accord with the laboratory impact experiments.

(ii) The second step is to model a steady-state distribution of dust around a parent moon. Given these ejecta production rate and initial distributions, a phase (space-velocity) distribution of grains in the vicinity of the body is found in closed form (Eq. (35)). The number density of dust at any point around the body is expressed in the form of a converging improper integral of the phase distribution function (Eq. (38)). This integral is taken in special functions or is evaluated in the form of series expansions. Simple approximate formulae, suitable for fast numerical estimates,

are given as well (Eqs. (42) and (53), in which the factors K_{bound} and $c_0 K_{\text{unbound}}$ are close to unity). Finally, an integral expression for the dust flux onto a dust detector with an arbitrary flyby trajectory and arbitrary angular sensitivity function (Eqs. (67) and (68)) is also derived.

(iii) We have shown, in particular, that the steady-state number density n well within the Hill's sphere of the parent body is dominated by particles in ballistic trajectories and decreases with the distance r from the body's center as $n(r) \propto r^{-\alpha}$, with $2 < \alpha \approx 2.5$. The number density of escaping grains slopes more gently, α being close to 2. The radial profile of the number density depends only weakly on the angular distribution of initial ejecta velocities.

An important remark is that the model presented in this paper assumes an isotropic, stationary impactor flux that produces a spherically symmetric, time-constant dust cloud around a body. These assumptions are only approximations to reality. For instance, orbital motion of the satellite with respect to the impactors would result in a non-uniform and time-dependent dust production from the surface and, as a consequence, in an asymmetric and time-variable dust density distribution in the dust cloud. These effects will be given full consideration in a subsequent paper.

6.2. Applications

Applications are made to Jupiter's moon Ganymede and six outer satellites of Saturn. In the former case, the model is shown to be consistent with the measurements of the Dust Detector System (DDS) onboard the Galileo spacecraft. In the latter case, estimates are given and recommendations are made for the planned measurements with the Cassini Cosmic Dust Analyzer (CDA) during targeted flybys of the spacecraft with the moons. Our specific findings for the Cassini CDA are as follows:

(i) The best CDA pointing is very close to the apex of Cassini motion with respect to a satellite (see Fig. 11).

(ii) With this pointing, Enceladus flybys will give very high impact rates, at least hundreds of hits per minute. The expected total number of impacts range from about 4000 for Enceladus-1 and -2 to about 20,000 for Enceladus-3. Note that the "background" impact rates of the E-ring particles near Enceladus *may* be comparable with those of the Enceladus cloud particles. The impact rates are also very high, ~ 100 min^{-1}, for Dione and Rhea. For Rhea-5500, Hyperion, and Phoebe, the probable impact rate at the closest approach is about one impact per minute, with the total of ten to several tens of hits per flyby. Thus detection of dust is extremely likely in all the cases except perhaps for Iapetus, where only a few impacts are expected. All absolute numbers (Table 4), although uncertain to at least one order of magnitude, are rather conservative. This applies especially to Enceladus and Hyperion where, in addition to usual interplanetary impactors, other populations of impactors may increase the ejecta production significantly.

(iii) The impact rate drops rapidly with increasing distance from the satellite, because so does the number density in a cloud (close to $\propto r^{-2.5}$, Eq. (42)). For instance, the impact rate at C/A with Rhea, $\sim 60 \text{ min}^{-1}$, reduces to $\sim 7 \text{ min}^{-1}$ five minutes before or after C/A. For small satellites, the impact rate drops even faster. For example, for the Enceladus-1 flyby, the impact rate reduces from ~ 600 to 40 min^{-1} at ± 5 min from C/A (Fig. 10). Therefore, measurements beyond several minutes from C/A would already be useless, except for the Enceladus flybys. For Enceladus, the "time window" around C/A may be $\sim \pm 20$ min. We warn, however, that the last estimate was made with the model that is not necessarily valid far from Enceladus, where the dust distribution can be tangibly modified by perturbing forces. Also, the expected strong "E-ring background" may narrow the "time window" considerably.

(iv) If the CDA symmetry axis is not directed along the Cassini velocity vector w.r.t. a moon, the impact rates will decrease (see Fig. 11). As the proper velocities of the dust grains in the clouds are small compared to the Cassini flyby velocities, this decrease is largely determined by the sensitivity curve of CDA as a function of the incidence angle. In particular, pointing within about $45°$ from the apex direction will still lead to the detection of dust by the impact ionization target.

The model can be readily applied to presumed dust clouds around other bodies and, accordingly, to provide useful guidelines for planning of dust measurements by other space missions. One example is the predicted dust cloud in the Pluto-Charon system that could be revealed by a future mission to the outer solar system (Thiessenhusen et al., 2002). Another, and probably the best example is the ejecta cloud around Mercury and the planned dust experiment aboard the BepiColombo mission (Müller et al., 2002). In many respects (mass of the body, almost undistorted spherical symmetry, dominance of interplanetary impactor population), the Mercury case is very similar to the case of the Galilean satellites, for which the model has been successfully tested against the dust data of the Galileo spacecraft.

Acknowledgements

References

Abramowitz, M., Stegun, I.A., 1970. Handbook of Mathematical Functions. Dover Publications, NY.

Asada, N., 1985. Fine fragments in high-velocity impact experiments. J. Geophys. Res. 90, 12,445–12,453.

Banaszkiewicz, M., Krivov, A.V., 1997. Hyperion as a dust source in the saturnian system. Icarus 129, 289–303.

Burns, J.A., Showalter, M.R., Morfill, G.E., 1984. The ethereal rings of Jupiter and Saturn. In: Greenberg, R., Brahic, A. (Eds.), Planetary Rings. University of Arizona Press, Tucson, pp. 200–272.

Burns, J., Hamilton, D.P., Mignard, F., Soter, S., 1996. The contamination of Iapetus by Phoebe dust. In: Gustafson, B.A.S., Hanner, M.S. (Eds.), Physics, Chemistry, and Dynamics of Interplanetary Dust, ASP Conference Series, Vol. 104. ASP, San Francisco, pp. 179–182.

Colombo, G., Lautman, D.A., Shapiro, I.I., 1966. The Earth's dust belt: fact or fiction? 2. Gravitational focusing and Jacobi capture. J. Geophys. Res. 71, 5705–5717.

Colwell, J.E., 1993. A general formulation for the distribution of impacts and ejecta from small planetary satellites. Icarus 106, 536–548.

Colwell, J.E., Horányi, M., 1996. Magnetospheric effects on micrometeoroid fluxes. J. Geophys. Res. 101, 2169–2175.

Cuzzi, J.N., Durisen, R.H., 1990. Bombardment of planetary rings by meteoroids—general formulation and effects of Oort Cloud projectiles. Icarus 84, 467–501.

Cuzzi, J.N., Estrada, P.R., 1998. Compositional evolution of Saturn's rings due to meteoroid bombardment. Icarus 132, 1–35.

Dikarev, V.V., 1999. Dynamics and spational distribution of particles in Saturn's E ring. Ph.D. Thesis, St. Petersburg University (in Russian).

Dikarev, V.V., Grün, E., 2002. New information recovered from the Pioneer 11 meteoroid experiment data. Astron. Astrophys. 383, 302–308.

Divine, N., 1993. Five populations of interplanetary meteoroids. J. Geophys. Res. 98, 17029–17048.

Gladman, B., Kavelaars, J.J., Holman, M., Nicholson, P., Burns, J., Hergenrother, C.W., Petit, J.-M., Mersden, B.G., Jacobson, R., Gray, W., Grav, T., 2001. Discovery of 12 satellites of Saturn exhibiting orbital clustering. Nature 412, 163–166.

Grün, E., Zook, H.A., Fechtig, H., Giese, R.H., 1985. Collisional balance of the meteoritic complex. Icarus 62, 244–272.

Grün, E., Baguhl, M., Fechtig, H., Hamilton, D.P., Kissel, J., Linkert, D., Linkert, G., Riemann, R., 1995. Reduction of Galileo and Ulysses dust data. Planet. Space Sci. 43, 941–951.

Hamilton, D.P., Burns, J.A., 1991. Orbital stability zones about asteroids. Icarus 92, 118–131.

Hamilton, D.P., Burns, J.A., 1992. Orbital stability zones about asteroids. II. The destabilizing effects of eccentric orbits and of solar radiation. Icarus 96, 43–64.

Hartmann, W.K., 1985. Impact experiments. 1. Ejecta velocity distributions and related results from regolith targets. Icarus 63, 69–98.

Humes, D.H., 1980. Results of Pioneer 10 and 11 meteoroid experiments—interplanetary and near-Saturn. J. Geophys. Res. 85, 5841–5852.

Jewitt, D., Luu, J., 1995. Kuiper Belt: collisional production of dust around main-sequence stars. Astrophys. Space Sci. 223, 164–165.

Juhász, A., Horányi, M., 2002. Saturn's E ring: a dynamical approach. J. Geophys. Res. 107, 10.1029/2001JA000182.

Kholshevnikov, K.V., Shor, V.A., 1994. Velocity distribution of meteoroids colliding with planets and satellites. Astron. Astrophys. Trans. 5, 233–241.

Kholshevnikov, K.V., Shor, V.A., 1995. Velocity distribution of meteoroids colliding with planets and satellites. II. Numerical results. Astron. Astrophys. Trans. 8, 49–58.

Kivelson, M.G., Warnecke, J., Bennett, L., Joy, S., Khurana, K.K., Linker, J.A., Russell, C.T., Walker, R.J., Polanskey, C., 1998. Ganymede's magnetosphere: magnetometer overview. J. Geophys. Res. 103, 19,963–19,972.

Koschny, D., Grün, E., 2001. Impacts into ice–silicate mixtures: crater morphologies, volumes, depth-to-diameter ratios and yield. Icarus 154, 391–401.

Krivov, A.V., Banaszkiewicz, M., 2001a. Dust influx to Titan from Hyperion. In: Marov, M.Y., Rickman, H. (Eds.), Collisional Processes

in the Solar System (Astrophysics and Space Science Library, Vol. 261). Kluwer, Dordrecht, pp. 265–276.

Krivov, A.V., Banaszkiewicz, M., 2001b. Unusual origin, evolution and fate of icy ejecta from Hyperion. Planet. Space Sci. 49, 1265–1279.

Krivov, A.V., Jurewicz, A., 1999. The ethereal dust envelopes of the Martian moons. Planet. Space Sci. 47, 45–56.

Krivov, A.V., Mann, I., Krivova, N.A., 2000. Size distributions of dust in circumstellar debris disks. Astron. Astrophys. 362, 1127–1137.

Krüger, H., Krivov, A.V., Hamilton, D.P., Grün, E., 1999. Detection of an impact-generated dust cloud around Ganymede. Nature 399, 558–560.

Krüger, H., Krivov, A.V., Grün, E., 2000. A dust cloud of Ganymede maintained by hypervelocity impacts of interplanetary micrometeoroids. Planet. Space Sci. 48, 1457–1471.

Krüger, H., Horányi, M., Krivov, A.V., Graps, A., 2002. Jovian dust: Streams, clouds and rings. In: Bagenal, F., McKinnon W., Dowling, T. (Eds.), Jupiter: The Planet, Satellites & Magnetosphere, Cambridge University Press, Cambridge, in press.

Meyer-Vernet, N., Lecacheux, A., Pedersen, B.M., 1996. Constraints on Saturn's E ring from the Voyager 1 radio astronomy instrument. Icarus 123, 113–128.

Müller, M., Green, S.F., McBride, N., Koschny, D., Zarnecki, J.C., Bentley, M.S., 2002. Estimation of the dust flux near Mercury. Planet. Space Sci., in press.

Showalter, M.R., Cuzzi, J.N., Larson, S.M., 1991. Structure and particle properties of Saturn's E ring. Icarus 94, 451–473.

Spahn, F., Thiessenhusen, K.-U., Colwell, J.E., Srama, R., Grün, E., 1999. Dynamics of dust ejected from Enceladus: application to the Cassini–Enceladus encounter. J. Geophys. Res. 104, 24,111–24,120.

Srama, R., Bradley, J.G., Grün, E., 2002. 26 colleagues The Cassini cosmic dust analyzer. Space Sci. Rev., in press.

Thiessenhusen, K.-U., Krivov, A., Krüger, H., Grün, E., 2002. Dust envelope of Pluto and Charon. Planet. Space Sci. 50, 79–87.

Tsintikidis, D., Kurth, W.S., Gurnett, D.A., Barbosa, D.D., 1995. Study of dust in the vicinity of Dione using the Voyager 1 plasma wave instrument. J. Geophys. Res. 100, 1811–1822.

Tublina, O.K., Kholshevnikov, K.V., 1991. Accretion rate onto a convex body. Proceedings of the Leningrad University, Series 1, No. 3 (15), pp. 128–130 (in Russian).

Yamamoto, S., Mukai, T., 1998. Dust production by impacts of interstellar dust on Edgeworth–Kuiper Belt objects. Astron. Astrophys. 329, 785–791.